https://doi.org/10.15407/ufm.23.03.438

P.E. MARKOVSKY [1,2,*], J. JANISZEWSKI [2], S.V. AKHONIN [3], V.I. BONDARCHUK [1], V.O. BEREZOS [3], K. CIEPLAK [2], O.P. KARASEVSKA [1,4], and M.A. SKORYK [1]

[1] G.V. Kurdyumov Institute for Metal Physics of the N.A.S. of Ukraine, 36 Academician Vernadsky Blvd., UA-03142 Kyiv, Ukraine
[2] General Jarosław Dąbrowski Military University of Technology, 2, General Sylwester Kaliski Str., PL-00-908 Warsaw, Poland
[3] E.O. Paton Electric Welding Institute of the N.A.S. of Ukraine, 11 Kazimir Malevich Str., UA-03150 Kyiv, Ukraine
[4] National Technical University of Ukraine 'Igor Sikorsky Kyiv Polytechnic Institute', 37 Peremohy Ave., UA-03056 Kyiv, Ukraine
* pmark@imp.kiev.ua, p_markovsky@yahoo.com

MECHANICAL BEHAVIOUR OF Ti–15Mo ALLOY PRODUCED WITH ELECTRON-BEAM COLD HEARTH MELTING DEPENDING ON DEFORMATION RATE AND IN COMPARISON WITH OTHER TITANIUM ALLOYS

Ti–15(wt.%)Mo alloy is produced with conventional cast and wrought approach using double electron-beam cold hearth melting, 3*D* hot pressing, and subsequent rolling. Three batches of specimens are subjected to microstructure study and quasi-static tensile testing in the following states: (1) as-rolled, (2) partially recrystallized *via* annealing at 800 °C for 40 minutes, (3) annealed at 800 °C for 3 hours followed by water quenching to fix the β-phase. The specimens in the second state (2) are chosen for more detailed study of mechanical behaviour upon both quasi-static and high strain-rate compressions. The obtained data on the mechanical behaviour are analysed from the standpoint of the effect of initial microstructure and crystallographic texture in three mutually perpendicular planes on the strain energy and the critical strain rate that results into fracture. A detailed microstructural study

Citation: P.E. Markovsky, J. Janiszewski, S.V. Akhonin, V.I. Bondarchuk, V.O. Berezos, K. Cieplak, O.P. Karasevska, and M.A. Skoryk, Mechanical Behaviour of Ti–15Mo Alloy Produced with Electron-Beam Cold Hearth Melting Depending on Deformation Rate and in Comparison with Other Titanium Alloys, *Progress in Physics of Metals*, **23**, No. 3: 438–475 (2022)

of the tested specimens reveals the influence of microstructure and texture on the deformation mechanisms at different strain rates. A strong effect of microstructural inhomogeneity and crystallographic texture formed during rolling is noted. The results are compared with those obtained earlier for other titanium alloys and some important structural materials tested under the same conditions. As shown, the Ti–15Mo alloy has a rather high mechanical characteristic. At high strain rates, this material corresponds to other single-phase titanium alloys in terms of strain energy; however, it is inferior to the two-phase alloys with a fine and homogeneous microstructure, *e.g.*, Ti-6-4 or T110 (see list of acronyms in Appendix). Taking into account the specific weight of materials, the Ti–15Mo alloy is not inferior to such high-strength materials as the heat-hardened alloy B95, steels ARMOX 600T and Docol 1500M, and, in addition, is cheaper compared to other titanium β-alloys.

Keywords: titanium beta-alloy, microstructure, crystallographic texture, mechanical properties, strain rates of deformation, deformation mechanism.

1. Introduction

Titanium based alloys are very important structural materials for a wide range of practical applications where high specific strength in combination with good ductility, fatigue strength, resistance to crack propagation, high corrosion resistance, and non-magnetic properties are required [1–4]. The metastable β-class alloys hold a special place among titanium based alloys due to their good workability (they can even be subjected to cold deformation), and the possibility of forming special highly dispersed microstructural states which provide a combination of high strength (more than 1500 MPa) with sufficiently high ductility [3–5]. High plasticity of these alloys is explained by the fact that, in contrast to the α- and α+β-alloys, both metastable (as-quenched) and stable β-alloys have a bcc elementary lattice with higher number of easy sliding crystallographic planes as compared to the hcp lattice of the α-phase [1, 2]. In addition, as shown in Ref. [6], the implementation of titanium β-matrix instead of α+β-one in the metal-matrix composites makes it possible to increase significantly the plastic characteristics of a material with rather low ductility. Otherwise, only unalloyed (pure-α) titanium was used to obtain sufficient level of plasticity in metal-matrix composites, which resulted in very low level of overall strength [7].

The Ti–15Mo binary alloy is one of the typical representatives of titanium-based β-alloys. Unlike most other commercial titanium alloys, it not only has a relatively simple chemical composition, but it is sufficiently resistant to both thermal and deformation influence in as-quenched (single β-phase) condition [8, 9]. Due to the combination of acceptable strength and high ductility, this alloy was tested as a material for medical applications, but it has not found wide application. At the same time, such combination of properties may be very attractive in the cases when high ductility is very important. For instance, there are

some experiments when the Ti–15Mo composition was used as a matrix for composites reinforced with TiC [10] or TiB [11] hard particles, which ensured higher ductility of these materials. However, neither the cast and wrought Ti–15Mo alloy itself nor metal-matrix composites based on it have so far been subjected to sufficiently detailed studies of the mechanical behaviour depending on the strain rate. In general, it should be noted that the mechanical properties of titanium β-alloys under dynamic loading are very poorly studied. Therefore, this work was concerned with a detailed study of the effect of strain rate on the mechanical behaviour of the Ti–15Mo alloy in as-cast and deformed, as well as heat-treated states under both tension and compression. In addition, the data obtained in this work were compared with those previously obtained for other alloys in order to determine the position of the Ti–15Mo alloy among industrial titanium alloys with different chemical and phase compositions from the standpoint of mechanical behaviour.

2. Material Preparation and Experimental Procedure

The Ti–15Mo alloy was produced by electron beam cold hearth double melting method using UE-208M multipurpose electron-beam unit equipped with three gas-discharge electron guns [12, 13]. Commercial purity titanium (Grade 2) and 99.9% purity molybdenum were used as raw materials. Melting was performed in a chamber under residual vacuum not lower than $6 \cdot 10^{-2}$ Pa. Cast ingot had 100 mm diameter and about 300 mm length. All subsequent thermomechanical and heat treatments are summarized in the diagram shown in Fig. 1. After the melting, the ingots were machined: head and bottom parts were cut off, and the side surfaces were machined. Next, the ingot was subjected to 3*D* hot pressing at 900 °C with a total reduction of at least 50%; then it was cross-rolled at 800 °C into a 10 mm thick plate. The melting and hot forming procedures were described in more detail in [12].

The obtained plate was cut into three parts for studying the material in three different microstructural states. The first part was assigned to as-rolled state (state #1). Two other parts were subjected to annealing at 800 °C with exposures for 40 minutes (state #2), and 3 hours (state #3). These exposures were chosen in order to achieve different conditions from the viewpoint of recrystallization completeness and final β-grain structure. After both exposures, the material was quenched in water to fix single-phase high-temperature β-condition. Then, two types of samples *I* and *II* were cut from states #1 and #3 (see Fig. 2) for microstructure and x-ray studies, and tensile tests, respectively. The samples of all three types (Fig. 2) were cut from the plate of state #2, and the samples of the type *III* were prepared in the three mutually perpendicular directions (*X*, *Y*, and *Z*) for compression tests.

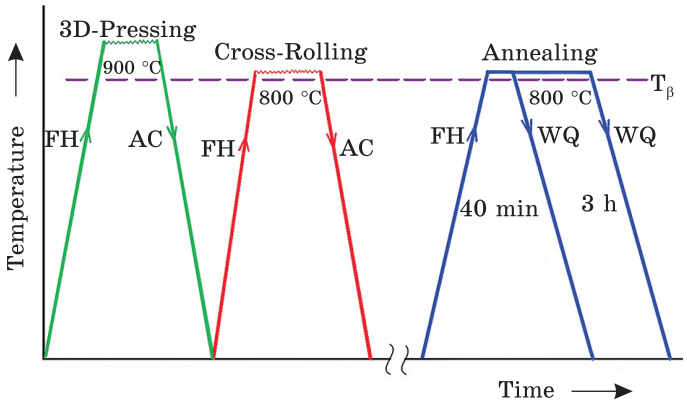

Fig. 1. The sequence of thermomechanical and heat treatments of Ti–15Mo alloy applied in the present study (scheme)

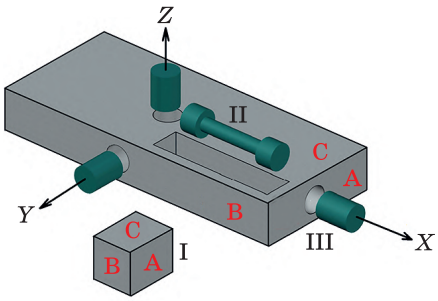

Fig. 2. Scheme of sampling for microstructure and crystallographic texture studies (*I*), and for mechanical tests: tension (*II*), and compression (*III*). *A*, *B*, and *C* — planes with different orientations with respect to rolling direction (RD — *X* axis)

Tensile tests were performed according to the ASTM E8 standard with specimens with 4 mm gage diameter and 25 mm gage length (samples *I* in Fig. 2) using INSTRON 3376 machine. Tension rates were varied from $8 \cdot 10^{-4}$ to $3.6 \cdot 10^{-2}$ s^{-1}. The quasi-static and high strain-rate compression tests were conducted on cylindrical specimens of 5 mm diameter and 5 mm length, which were cut in three mutually perpendicular directions (samples *III* in Fig. 2). The high strain-rate compression tests were performed by means of the classical split Hopkinson pressure bar (SHPB) technique [14, 15] using the scheme described in detail in our previous works [16, 17]. The compression rate was 10^{-3} s^{-1} in the QSC tests, whereas in the SHPB experiments it varied from 1420 to 3280 s^{-1}. The structure of all materials was studied with light microscopy (LM) at an XL70 (Olympus, Japan) microscope, and scanning electron microscopy (SEM) at VEGA3 and MIRA3 microscopes (both TESCAN, Czech Republic). The maps of local orientations of some samples in different states were obtained by means of electron backscatter diffraction (EBSD) technique at MIRA3 SEM. Fine microstructure in a heavily deformed zone of a tensile specimen was studied with TEM using JEOL-2000CX (Japan) microscope. The phase composition and crystallographic texture were examined by x-ray diffraction analysis at an ULTIMA IV (RIGAKU, Japan) diffractometer.

Experimental data for other titanium alloys, Ti–6(wt.%)Al–4V, T110 (Ti–3.9Al–0.8V–1.5Mo–2.1Fe–0.7Zr–3.8Nb), TIMETAL-LCB (Ti–

3Al–4.5Fe–6.8Fe), VT22 (Ti–5Al–5V–5Mo–1Fe–1Cr), and 'gum metal' (Ti–36Nb–2Ta–3Zr–0.3O), were obtained by the authors and discussed in the previous works [16–23]. In the present work, we used some results on the mechanical properties of these materials; values of strain energy of TIMATEL-LCB and 'gum metal' were recalculated and compared with those for Ti–15Mo. Thus, the data were summarized, and general behaviour of both single-phase α- or β-, and two-phase α+β commercial titanium alloys was revealed depending on the test method and loading rate.

3. Experimental Results

3.1. Microstructure and Hardness in As-Rolled and Recrystallized + Water Quenched States

In the initial state, the microstructure of the alloy comprised of flattened and elongated in the rolling direction grains that formed parallel bands in the *X*-plane (Fig. 3, *a*, *b*). It is important to underline that the density of deformation defects in different bands was different. Most likely, this is due to different lattice orientation in neighbouring β-grains in respect to applied loading, which caused varying number of planes of easy sliding activated during deformation. This structural inhomogeneity was accompanied by a rather significant difference in hardness: the bands with low defect density had 267–292 *HV*, whereas the hardness of highly deformed ones reached 335 *HV*.

Heating to the temperatures of the single-phase β-region (above T_β = 745 °C) led to the initiation of recrystallization processes. However, even holding at 800 °C for 40 minutes (followed by water quenching to prevent the earliest stages of the metastable β-phase decomposition) did not lead to complete recrystallization of the entire volume of the alloy (this is well seen in plane *B* along *X*-axis, Fig. 3, *c*, *d*). That is, after this heat treatment, both areas (bands) of rather fine recrystallized β-grains (indicated by *I* with an arrow in Fig. 3, *c*) and completely non-recrystallized bands (indicated by *II* with an arrow in Fig. 3, *c*) are simultaneously present. Apparently, this is caused by the inhomogeneous distribution of deformation defects over the grains: normal recrystallization (*via* nucleation and further growth of new grains) took place in the grains with high concentration of defects, whereas in less deformed grains the processes did not go beyond the stages of recovery and/or polygonization, or so-called '*in situ*' recrystallization [24, 25].

In other two planes *A* (along axis *Y*, Fig. 3, *e*) and *C* (along axis *Z*, Fig. 3, *f*), the microstructure is somewhat different from that observed in the *B* plane. In the *A* plane, the bands with recrystallized grains look rather similar to those in the *B* plane (compare layers *I* in Fig. 3, *e* and *c*). As for non-recrystallized grains, they look not as continuous elon-

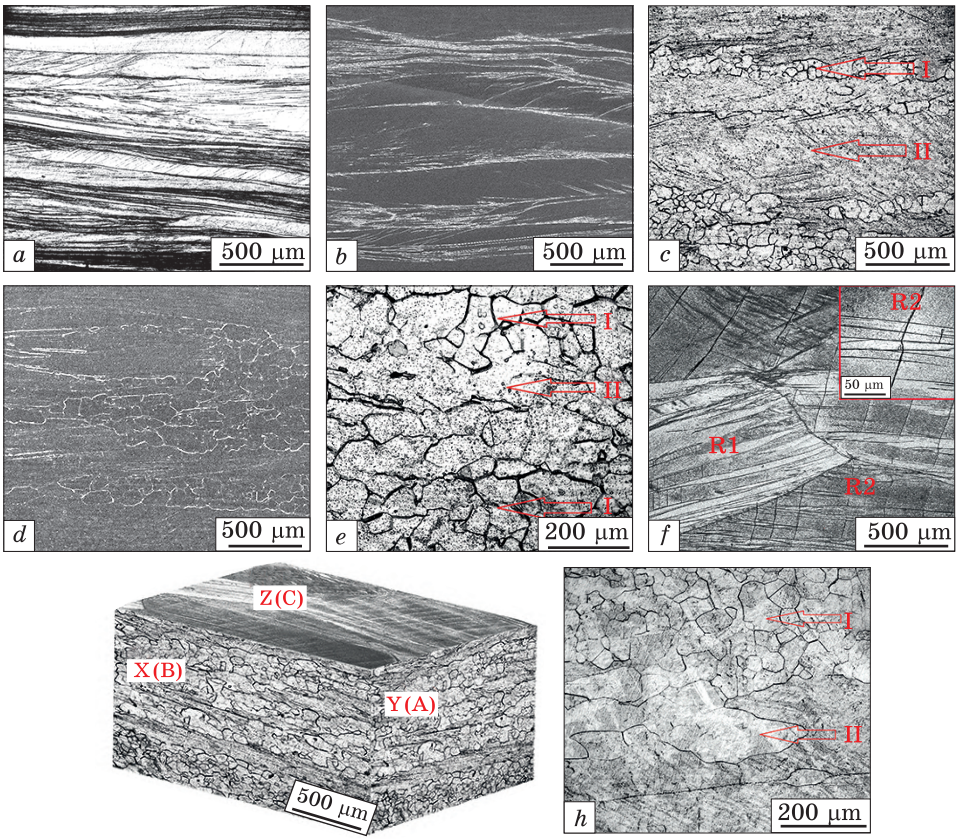

Fig. 3. Microstructure (along RD, direction *X* in Fig. 2) of Ti–15Mo alloy in as-rolled state #1 (*a*, *b*), annealed at 800 °C for 40 min state #2 (*c*–*f*), and 3 hours state #3 (*h*). The microstructure was studied along directions (*a*–*d*, *h*) *X* (plane *B*), (*e*) *Y* (plane *A*), and (*f*) *Z* (plane *C*). Here, *g* — 3*D* representation of the state #2; *a*, *c*, *e*, *f*–*h* — LM; *b*, *d* — SEM, SEI. Roman numerals and arrows in *c*, *e*, and *h* denote the bands formed due to nucleation and recrystallization growth of new β-grains (*I*) and polygonization or secondary recrystallization (*II*)

gated layers in the *A* plane, but as separate somewhat flattened grains (*II* in Fig. 3, *e*). The microstructure in the *C* plane strongly depends on the zone where the material was cut (either *I* or *II*). For instance, Fig. 2, *f* represents the microstructure in the zone *II*. This figure clearly shows a longitudinal section of several neighbouring flat grains from the *II* layer in Fig. 3, *e*, stretched in the rolling direction, with a complex intragranular substructure. The latter comprises of both slip bands (region *R*1) and some combination of slip bands and possibly twins (region *R*2). The 3*D* visualization of the microstructures in individual planes (*A*, *B*, and *C*, as well direction along axis *X*, *Y*, and *Z* in Fig. 2) is shown in Fig. 3, *g*.

Taking into account the general laws, which govern the relaxation of deformation defects (including recrystallization) in these materials [24, 26], it can be assumed with sufficient confidence that it is necessary to increase either the isothermal exposure time or the recrystallization temperature to form a completely recrystallized state. In this case, a completely recrystallized microstructure will be formed due to the collective growth of neighbouring β-grains until the complete absorption of unrecrystallized gaps between them [24, 25]. However, as can be seen from Fig. 3, *c* and *d*, already formed β-grains are rather coarse (>100 μm) that means that further increase in the temperature or the annealing time will lead to further growth of β-grains, which can reach 500 μm or more in diameter upon 3 h exposure (Fig. 3, *h*). Those bands where recrystallization did not begin by the mechanism of nucleation and growth of new β-grains at a relatively short exposure (40 minutes), most likely underwent transformation by the mechanism of recovery or '*in situ*' recrystallization (compare Figs. 3, *c*, *d* with 3 h) with the disappearance of low-angle boundaries between neighbouring slightly misoriented subgrains [27, 28]. This specific mechanism of recrystallization led to forming the regions with different grain sizes that resulted in certain local differences in hardness. Three-hour annealing led to levelling of hardness in the zones with relatively fine recrystallized grains (280–290 *HV*) and those where polygonization or secondary '*in situ*' recrystallization occurred (288 *HV*). Somewhat higher hardness (310 *HV*) was observed inside the small and rather sparse areas with the finest β-grains preserved, in accordance with the Hall–Petch relationship $\sigma_T = \sigma_0 + Kd^{-1/2}$.

Thus, the presence of incompletely recrystallized microstructure after annealing for 40 minutes prevented complete elimination of the difference in the hardness in different zones. As expected, new recrystallized β-grains had a lower hardness (261 *HV* on the average), but the hardness of some non-recrystallized layers increased in some cases up to 315 or even 346 *HV*, possibly due to work hardening during quenching as a result of the difference in temperature expansion–compression coefficients in respect to the recrystallized areas. Therefore, although the recrystallization annealing made it possible to form a single-phase β-state, it did not eliminate completely the inhomogeneity in the microstructure and properties of the alloy. Nevertheless, as it was shown in several previous works, structurally inhomogeneous (including gradient [29]) or multilayer [30–32] materials are useful for certain applications; in most cases, such materials are produced with rather complicated technological methods. Hence, the material similar to that shown in Fig. 3, *c*–*g* is also of certain interest from the standpoint of its mechanical behaviour under quasi-static and dynamic loading.

In other words, a relatively short-term recrystallization annealing led to the formation of a 'natural' multilayer material with alternate

stronger and softer layers, due to the above-described features of the localization of deformation and recrystallization processes.

3.2. Phase Composition, Crystallographic Texture,and Residual Stresses

Detailed study of phase composition, residual stresses, and general crystallographic texture was performed with x-ray diffraction analysis on samples of two states, #1 (as-rolled) and #2 (short-time annealed, partially recrystallized). In both cases, single-phase β-state was detected (Fig. 4, *a*, *b*), although in some works the possibility of the formation of the ω-phase in this alloy was also noted (*e.g.*, upon quenching from

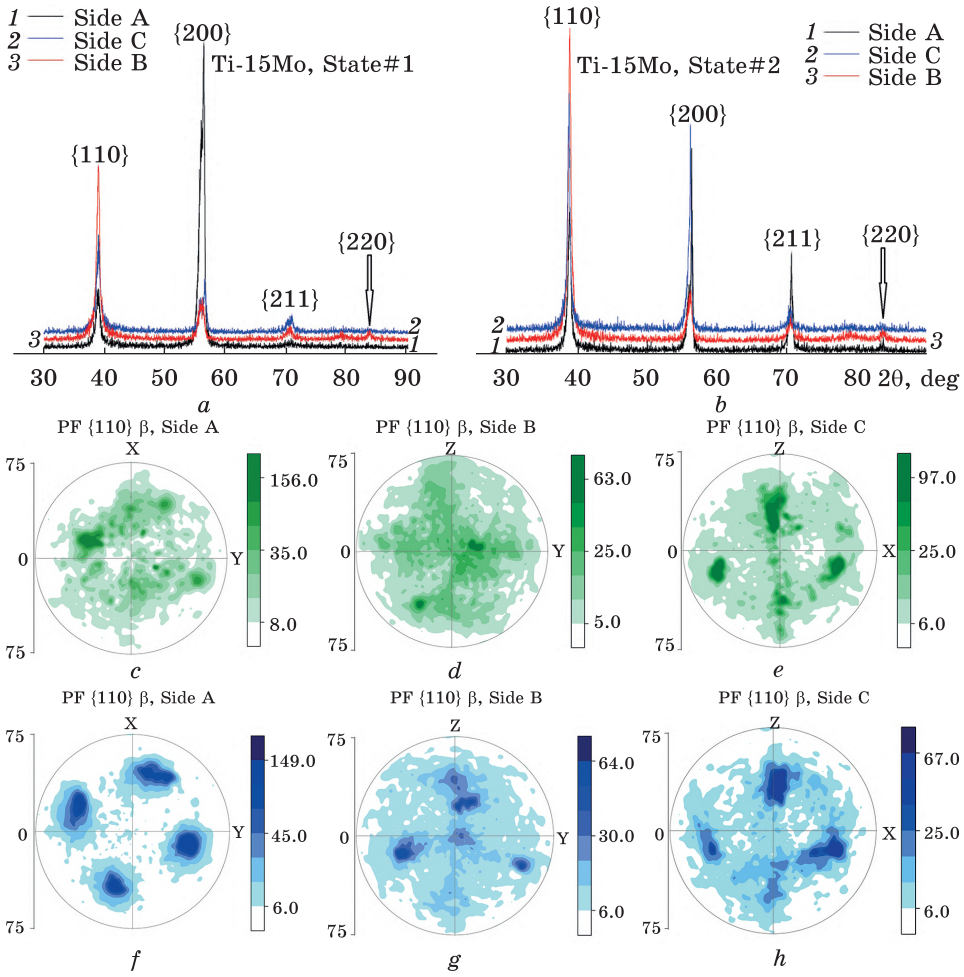

Fig. 4. XRD patterns (*a*, *b*) and {110}β pole figures (*c*–*h*) of Ti–15Mo in the states (*a*, *c*–*e*) #1 (as-rolled) and (*d*, *f*–*h*) #2 (partially recrystallized)

Table. **Measurement details used for calculations of deformation by reflexes shift**

	2Θ	FWHM	2Θ	ε, %	
(100)	{110}		{200}		
Ti–15Mo (sample #1)					
side *A*					
d = 3.26074485	39.03128 19.51564 0.33406416 *d* = 2.30569	0.52541	56.49145 28.245725 0.47325394 *d* = 1.62756 1.630372	–0.07% Compression	
side *B*					
d = 3.2579238	39.06497 19.5325 0.3343415 *d* = 2.30378	0.50675	56.21097 28.105485 0.47109633 1.6350159 1.62896	0.37% Tension	
side *C*					
d = 3.2683168	38.93713 19.4686 0.33329021 2.31104898	0.45233	56.28234 28.14117 0.47164561 1.63311177 1.6341584	–0.064% Compression	
Ti–15Mo (sample #2)					
side *A*					
d = 3.269931	38.91711 19.4586 0.33312565 *d* = 2.31219061	0.93555	56.09871 28.049355 0.47023197 1.6380213 *d* = 1.634965	0.97486	
side *B*					
d = 3.2680747	38.94024 19.4701 0.33331489 *d* = 2.3108778	0.60837	55.92756 27.96378 0.46891331 1.642627 1.634037	1.16084	
side *C*					
d = 3.264626	38.98307 19.4915 0.33366701 *d* = 2.308439	0.77974	56.27459 28.137295 0.47158598 1.633318 1.632313	1.30748	

inside samples #1 and #2

FWHM	2Θ	FWHM	ε, %	$\varepsilon_{aver.}$, %
	{211}			
Ti–15Mo (sample #1)				
side *A*				
0.36979	70.72775 35.363875 0.57876712 1.3308438 1.3311935	0.55154	–0.026% Compression	–0.05% Compression ACS 130 Å
side *B*				
0.83269	70.66281 35.331405 0.57830488 1.3319099 1.330042	0.77177	0.44% Tension	0.40% Tension ACS 175 Å
side *C*				
0.49957	70.56363 35.281815 0.57830488 1.3319099 1.33428475	0.60251	–0.078% Compression	–0.07% Compression ACS 167 Å
Ti–15Mo (sample #2)				
side *A*				
0.00305 0.187% Tension	70.59089 35.295445 0.57779274 1.33309 d = 1.33494374	1.33264	–0.0018 –0.13% Compression	0.02% Tension ACS 70 Å
side *B*				
0.21% Tension	70.49286 35.24643 0.57709431 1.3347038 1.3341859	1.15258	0.26% Tension	0.23% Tension ACS 101 Å
side *C*				
0.001 0.06% Tension	70.59742 35.29871 0.57783925 1.332983 1.33277798	1.29375	$2.05 \cdot 10^{-4}$ 0.015% Tension	0.04% Tension ACS 72 Å

the single-phase β-field [33, 34]). It should be noted that the intensity of the reflections (110) and (200) on the diffraction patterns registered from different surfaces (*A*, *B*, and *C*; see Fig. 2) of the samples differed quite strongly, and this difference was not the same for the states #1 and #2. Only this fact indicates the presence of a rather strong texture formed upon deformation and somewhat transformed due to partial recrystallization during annealing. Subsequent texture studies confirmed this, see Fig. 4, *c*–*h*.

First of all, it should be emphasized that the textures of similar type with pronounced 4 maxima located approximately at 60° with respect to each other were observed on all three surfaces (Fig. 4, *c*–*h*). In comparison with annealed state #2, as-rolled state #1 has more diffused maxima, compare the corresponding pairs for surfaces *A* (Fig. 4, *c* and *f*), *B* (Fig. 4, *d* and *g*), and not as much *C* (Fig. 4, *e* and *h*). It can also be noted that the maximum intensities of reflections somewhat decreased on each surface after annealing. Although the general type of the textures remained the same, the annealing triggered relaxation processes and partial recrystallization that caused the appearance of much more pronounced and sharper textures for surfaces *A* and *B* (Figs. 4, *c vs. f*, and *d vs. g*, respectively). As for the surface *C*, the texture looks unchanged, obviously because in both states (#1 and #2) the studied surfaces corresponded to the layers cut of coarse β-grains flattened in the rolling direction (as shown in Fig. 3, *f*).

The obtained data also made it possible to determine the residual macro- and microstresses, as well as the coherent scattering regions (CSRs). All measurement details used for calculations are presented in Table. The macro- and microstresses were estimated by the reflex shifts and by the reflex broadening using Williamson–Hall method, respectively [35, 36]. Tensile macrostresses are observed on the surfaces *B* of both samples, while the stresses on the surfaces *A* and *C* are an order of magnitude lower (the reflexes are shifted due to the deformation). According to calculations made for the surface *B* of the state #1, residual deformation is of about 0.20–0.25%, and residual macrostress can reach about 800 MPa, while in the state #2 the macrostresses are twice lower.

The microstresses are also twice higher in the state #1 compared to the state #2. These stresses are about 1/3 of the macrostresses. The size of the CSRs in the state #1 on the surface *B* is ≈175 Å; on the surfaces *A* and *C*, it is of 130 and 160 Å, respectively The size of the CSRs in the sample #1 on the surface *B* is ≈100 Å; on the surfaces *A*, *C*, it is of ≈70 and ≈72 Å, respectively.

3.3. Tension

Tensile tests were performed with specimens cut out along X axis (in RD direction) of the alloy in all three microstructural states, namely state #1 (as-rolled), state #2 (annealed for 40 minutes), and state #3 (annealed for 3 hours). Typical tensile curves are shown in Fig. 5 for two quasi-static strain rates. It is clearly seen that the material in the initial as-rolled state #1 is highly hardened by previous deformation, *i.e.*, ultimate tensile strength reaches 1200 MPa, but, after UTS, the flow stress sharply drops (Fig. 5, *a*). An increase in the deformation rate from $8 \cdot 10^{-4}$ s^{-1} to $4 \cdot 10^{-3}$ s^{-1} had negligible effect on the level of strength and ductility of the alloy work-hardened by rolling (curve *2 vs.* curve *1* in Fig. 5, *a*).

Partially recrystallized material after annealing at 800 °C for 40 min and water quenching (state #2) had UTS of only about 800 MPa that was reached after a fairly prolong deformation with noticeable hardening upon tension (Fig. 5, *b*). Moreover, in this case, the ductility of the alloy was many times higher than in as-rolled state #1, and the elongation was as high as about 40% at the lower strain rate (Fig. 5, *b*, curve *1*). The 5 times increase in strain rate reduced the ductility of the alloy without a noticeable strength change (UTS remained the same, while YS somewhat increased, compare curves *2* and *1*). However, these differences in ductility can also be explained by rather high heterogeneity of both the microstructure in this state (Fig. 3, *c*, *d*) and the above-mentioned variations in the hardness of different (recrystallized and not recrystallized) layers. It is likely that such a microstructure inhomogeneity manifested in the varying ratio of different layers in the specimens prepared for tensile tests also caused the observed variations in the elastic modulus, and so in the slope of the straight Hook's elastic parts of the tensile curves (compare curves *1* and *2* in Fig. 5, *b*).

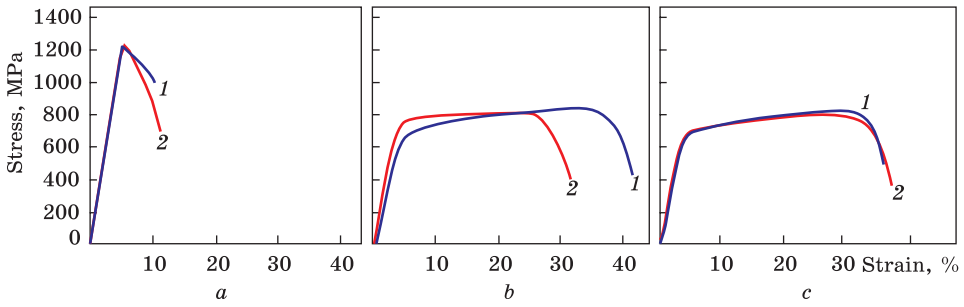

Fig. 5. Typical examples of engineering stress–strain curves for Ti–15Mo alloy in the states (*a*) #1 (as-rolled), (*b*) #2 (partially recrystallized after annealing 800 °C, 40 min), and (*c*) #3 (after annealing 800 °C, 3 h). Tension rates are $8 \cdot 10^{-4}$ s^{-1} (*1*) and $4 \cdot 10^{-3}$ s^{-1} (*2*)

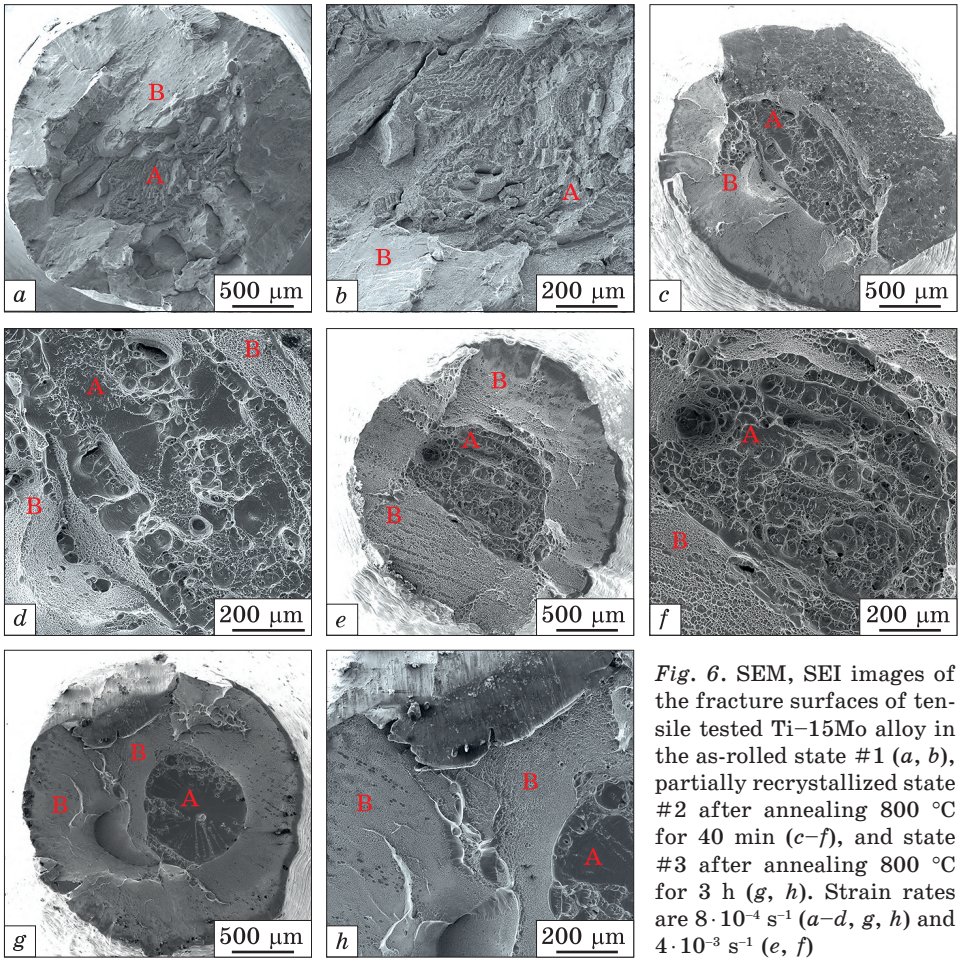

Fig. 6. SEM, SEI images of the fracture surfaces of tensile tested Ti–15Mo alloy in the as-rolled state #1 (*a*, *b*), partially recrystallized state #2 after annealing 800 °C for 40 min (*c*–*f*), and state #3 after annealing 800 °C for 3 h (*g*, *h*). Strain rates are $8 \cdot 10^{-4}$ s^{-1} (*a*–*d*, *g*, *h*) and $4 \cdot 10^{-3}$ s^{-1} (*e*, *f*)

After more prolonged annealing (3 hours, state #3), the alloy had more uniform properties at both strain rates, with almost identical tensile curves (Fig. 5, *c*).

Hence, comparing the microstructural states after annealing for different times, it can be concluded that longer annealing resulted in more equalized mechanical properties (hardness, strength, and plasticity), although it did not lead to the formation of a completely recrystallized structure of β-grains. After short annealing for 40 minutes, the alloy comprised two types of layers very different in structure and properties, which was confirmed at least by hardness measurements. Such a 'striped' material can be considered as a kind of layered composites with alternating softer and harder layers, which are often produced with rather complex technological approaches.

3.4. Fractography of Tensile Specimens

Fracture surfaces of the samples tested at various strain rates revealed a decisive effect of the layered structure (compare Fig. 3, *c* and *d* with Fig. 6). This effect was especially pronounced in the zone of delamination (in the centre of the specimens, *A*). At the same time, the areas of intense plastic flow (the edges of the fracture surfaces indicated by *B*) had very fine dimpled structure. In addition, the fracture surfaces of the specimens tested in the initial (as-rolled) state (Fig. 6, *a*, *b*) drastically differed from those of the annealed specimens (Fig. 6, *c*–*h*). In the latter case, fragments of brittle cleavage of different size were observed in both regions *A* and *B*.

After 40-minute annealing with a partial recrystallization, ductile dimples are observed; they are coarser in the centre of the specimens, and finer at the edges (Fig. 6, *c*–*f*). This can be explained by different mechanisms of deformation: the edges were subjected to intense local plastic deformation during neck formation, while the central part experienced uniform plastic flow only. As a result, in the central part fractured by rupture after relatively moderate deformation, and the banded structure of β-grains inherited after rolling revealed in this part of the fracture surface. An increase in the strain rate from $8 \cdot 10^{-4}$ s^{-1} to $4 \cdot 10^{-3}$ s^{-1} did not lead to a noticeable change in the type of fracture (compare Figs. 5, *c*, *d* with 6, *e*, *f*). In turn, the increase in the annealing time up to 3 hours noticeably changed the nature of the fracture; at the edges, the size of the ductile dimples decreased significantly (zone *B* in Fig. 6, *g*, *h*), obviously due to the absence of residual stresses. It is worthwhile to note that the coarse β-grain in the centre was apparently torn off completely (zone *A* in Fig. 6, *g*, *h*).

3.5. Compression

Figure 7 represents the results of compression tests performed in three mutually perpendicular directions with specimens of three types (see Fig. 2). Comparison of the curves for different directions shows, firstly, that in the *Y* and *Z* directions (Figs. 7, *b* and *c*, respectively), the levels of both plastic flow stress and plasticity monotonously increase with strain rate.

The main difference between the *Y* and *Z* directions consists in the fact that higher strain rates resulted predominantly in increase of the true strain values in the first case, whereas in the second case the strength increased. Besides, the specimens cut along the *Z* direction fractured at noticeably lower strain rate (2730 s^{-1} *vs.* 3280 s^{-1} for *Y* specimens). As for the *X* direction, the strain also increased rather monotonically with strain rate (Fig. 7, *a*). However, the strength characteristics did not change regularly with strain rate increase. Both UTS

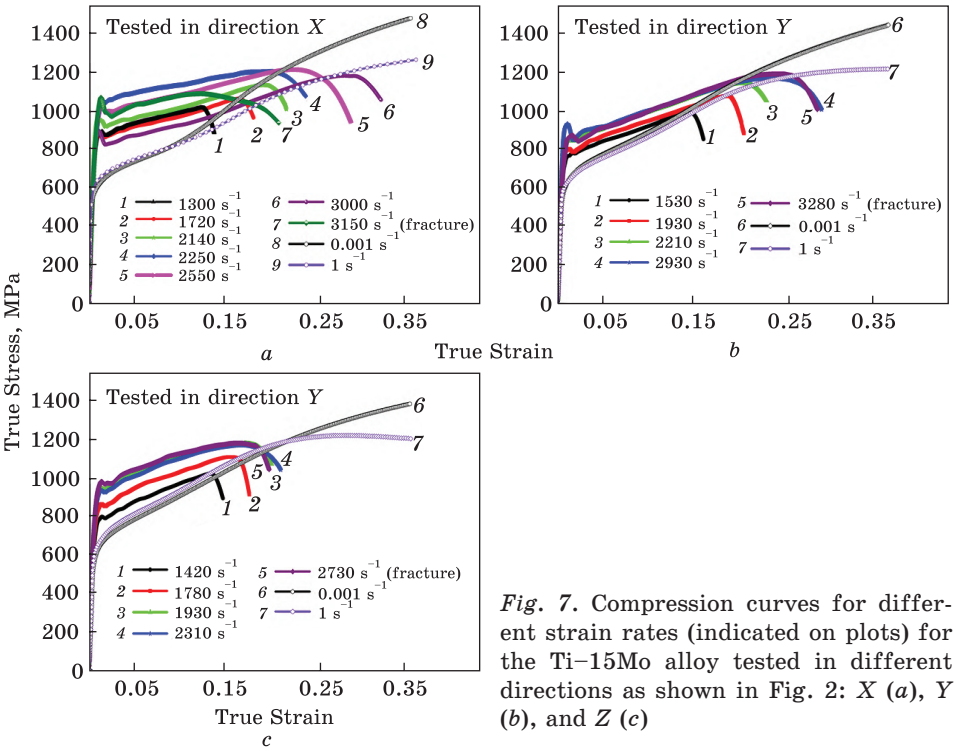

Fig. 7. Compression curves for different strain rates (indicated on plots) for the Ti–15Mo alloy tested in different directions as shown in Fig. 2: *X* (*a*), *Y* (*b*), and *Z* (*c*)

and the strength at stress peaks changed randomly in the range over 200 MPa. These differences in mechanical behaviour were obviously caused by the peculiarities of the crystallographic texture formed upon rolling (Fig. 4), as well as by the microstructure inhomogeneity after short-term recrystallization annealing (Fig. 3).

4. Discussion

As it was clearly shown in our previous works [16, 17], in order to reveal the main regularities in the effect of the structure, texture, and strain rate on the mechanical behaviour of titanium alloys, first of all, it is necessary to reveal in detail the features of the microstructure formed after loading.

4.1. Microstructure and Local Crystallographic Texture of a Tensile Tested (in Longitudinal X Direction) Specimen

The study of a Ti–15Mo tensile tested specimen revealed the presence of 3 zones with significant differences in microstructure (Fig. 8, *a*): zone *1* — unstrained initial state (see Fig. 3, *c*, *d*); zone *2* where relatively uniform plastic flow took place; and region *3* with intensive plastic localized deformation (neck formation). The material in zone *1* was in

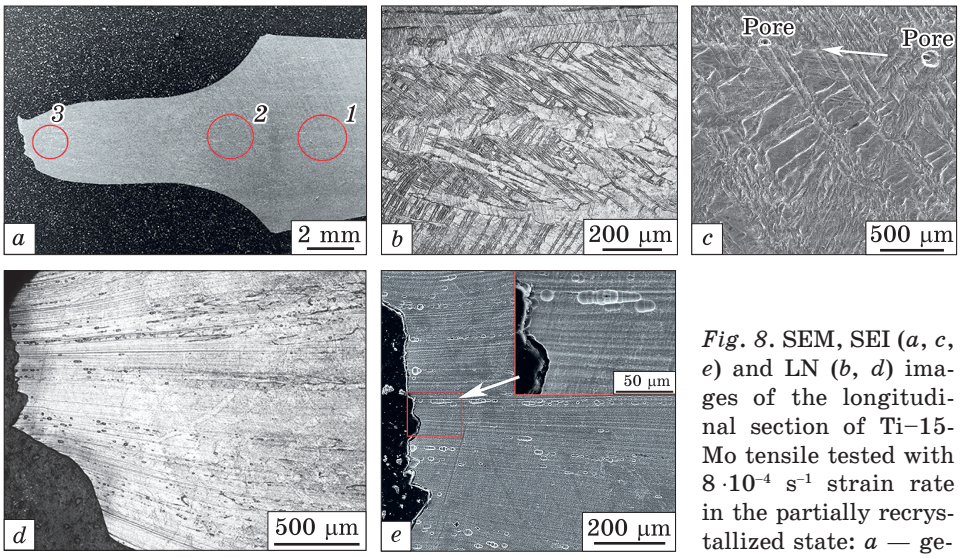

Fig. 8. SEM, SEI (*a*, *c*, *e*) and LN (*b*, *d*) images of the longitudinal section of Ti–15-Mo tensile tested with $8 \cdot 10^{-4}$ s^{-1} strain rate in the partially recrystallized state: *a* — general view with indicated specific zones; *b*–*e* — microstructure in the zones *2* (*b*, *c*) and *3* (*d*, *e*). Arrow (*c*) indicates boundary between two neighbouring grains

not-deformed state; its microstructure is shown in Figs. 3, *c*–*g*. The traces of plastic deformation become evident only in the transition zone *2* (Fig. 8, *b*, *c*). They look like either mutually intersecting slip bands or twins. In addition, separate pores are seen between neighbouring β-grains after etching (Fig. 8, *c*). In the zone of intense deformation (*3*), parallel slip bands are already observed, their internal structure cannot be revealed (Fig. 8, *d*, *e*). In this case, the bands certainly have deformation nature. The etched pores form continuous chains along the boundaries of neighbouring grains (Fig. 8, *e*). Separate pores come out to the fracture surface, while remaining locally dense grain boundaries form the edges of etch pits on them (Fig. 6, *f*).

The results of EBSD study performed on the same tensile tested specimen (see Fig. 8) are shown in Fig. 9. Inside the zone *1* that corresponds to initial (not deformed condition) of the state #2, the same two distinct regions *I* and *II* are clearly seen (compare Fig. 9, *a*, *b* with Fig. 3, *c*). The 1st of them (Fig. 9, *a*) consists of separate comparatively fine new β-grains that appeared upon recrystallization; most of these grains have rather high misorientation (*e.g.*, see grains *A*, *B*, and *C* in Fig. 9, *b*). Grain contours map of the same area (Fig. 9, *c*) illustrates distinct boundaries between these β-grains formed during recrystallization, while in the non-recrystallized regions *II* less clearly definedsub-boundaries can be observed (*e.g.*, those indicated by black arrows in Fig. 9, *c*).

In the zone 2, the above-mentioned substructure comprised of either mutually intersecting slip bands or twins was observed, because of plas-

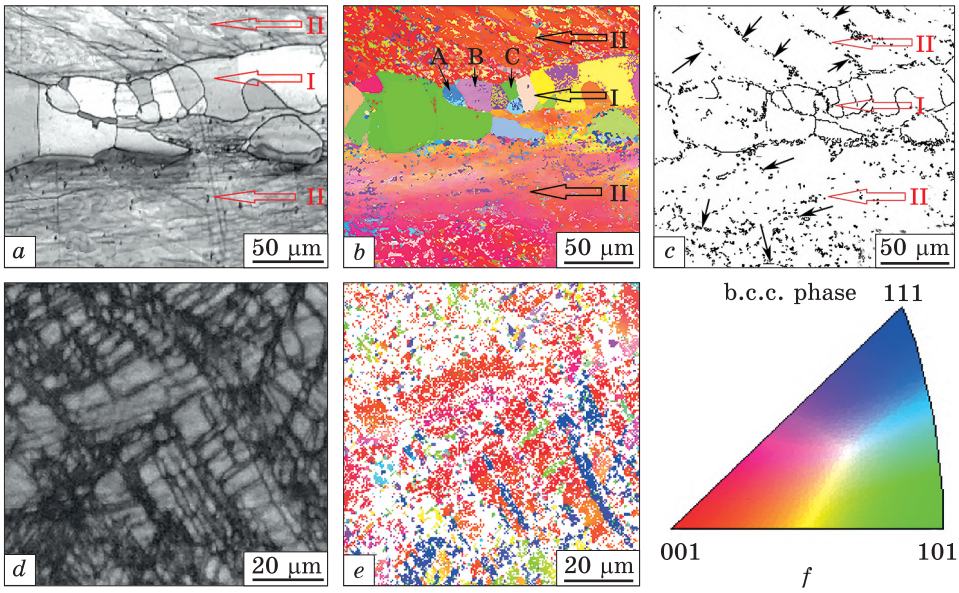

Fig. 9. SEM (a, *d*) and EBSD (*b*, *e*) data and grain contours map (*c*) for Ti–15Mo tensile tested specimen in the areas *1* (*a*–*c*) and *2* (*d*, *e*) from Fig. 8, *a*; *f* — inverted pole figure (crystallographic triangle). Romanian numbers and horizontal arrows (*a*–*c*) indicate bands similar to those in Fig. 3, *c*

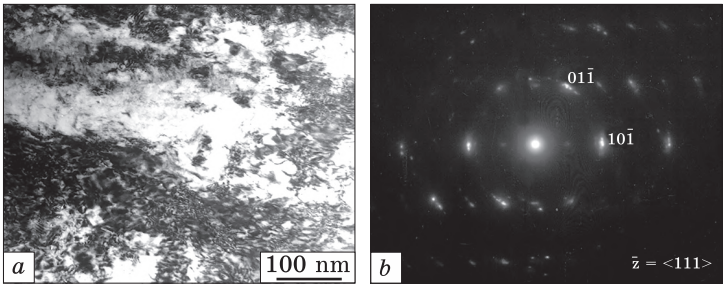

Fig. 10. TEM images of Ti–15Mo tensile tested specimen in the zone *3* (from Fig. 7, *d*, *e*), where *a* — bright field image, *b* — selected area diffraction pattern

tic deformation (Fig. 9, *d*). Unfortunately, the resolution of EBSD images in this area was much lower: about 40% of points were not identified (Fig. 9, *e*). Apparently, this is explained by inferior quality of the Kikuchi patterns taken from the microvolumes that underwent high local deformation, due to significant distortions caused by high defect density and high residual stresses [37]. However, the information obtained demonstrates that the identified areas between the unidentified ones have almost the same crystallographic orientation (Fig. 9, *e*). From all of the above, it can be concluded with a high probability that the

bands observed in Figs. 9, *d*, 8, *c*, and 8, *d* are the plastic slip bands, not twins. It should be noted that in the β-alloy of the same Ti–Mo system, although with a slightly lower content of molybdenum, twinning was observed along with the formation of deformational α″-martensite during plastic deformation [38].

As for zone *3*, it was not possible to obtain reliable results there also due to intense plastic deformation. Therefore, a foil was cut of this zone and prepared for TEM study which revealed a high density of deformation defects (Fig. 10, *a*), as well as preserved single-phase β-state and some broadening of the β-phase reflections due to these defects (Fig. 10, *b*). It should be noted that very similar situation was observed in other titanium β-alloys with different chemical compositions, which were subjected to various types of severe plastic deformation (about 99% reduction) at room temperature [39, 40].

4.2. Fracture Surfaces and Microstructure after Compression. Quasi-Static Tests

Typical microstructures of specimens QSC tested in different directions are presented in Fig. 11. Their comparison shows that the plastic flow of such a textured single-phase material is highly dependent on the relationship between the directions of texture and applied stress. For instance, compression along *X*-axis led to distortion of the elongated β-grains formed during the rolling, which is most evident near the edges of the specimen, where the plastic deformation was the highest (Fig. 11, *a*). No decomposition of β-phase was observed anywhere, only the grain boundaries were well contoured after etching (Fig. 11, *b*).

The compression along *Y*-axis led to higher distortion of the microstructural elements near the edges of the specimen (Fig. 11, *c*). Taking into account that the main direction of elongation of the β-grains is perpendicular to the page plane, both the boundaries of individual grains and subgrain boundaries inside them are seen (Fig. 11, *d*).

The compression along *Z*-axis caused the most pronounced deformation substructure (Fig. 11, *e*). As the external stress was applied in the same direction as during the previous rolling, further flattening of the elongated β-grains occurred. In this case, ‘cross-like’ pattern of microstructure typical for forging deformation scheme was observed with planes of sign-alternating shifts [41] due to the localized deformations in accordance with Schmid’s law. The most significant difference was observed in the level of plastic deformation of different layers (neighbouring β-grains with different crystallographic orientations), which led to the formation of extrusions and intrusions on the lateral surface of the specimen (Fig. 11, *f*).

Microstructures of the specimens SHPB tested with different strain rates in three mutually perpendicular directions are presented in

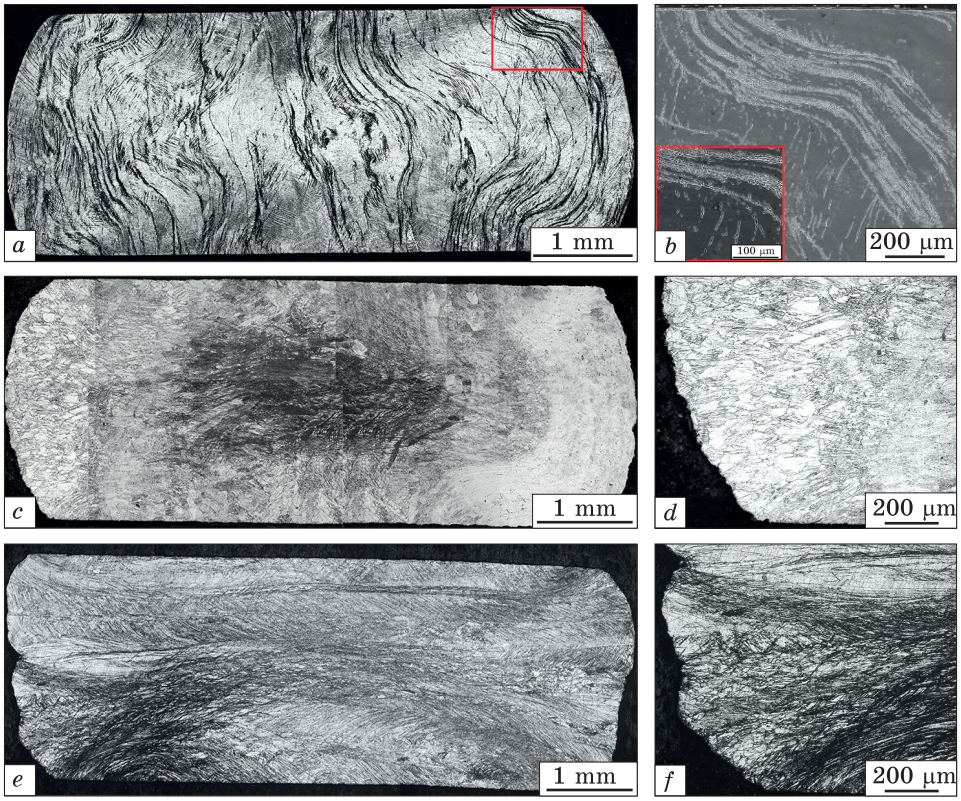

Fig. 11. The LM (*a*, *c*–*e*) and SEM (*b*) images of the microstructure of QSC tested specimens along the *X* (*a*, *b*), *Y* (*c*, *d*), and *Z* (*e*, *f*) axes

Figs. 12–14. First of all, it should be noted that the difference in strain rates between not cracked and cracked specimens was very small and did not exceed a few percent. For example, compression along *X*-axis with a rate of 3000 s^{-1} did not cause noticeable changes, particularly in grain structure (Fig. 12, *a*). Some barrelling was observed at one side only that is explained by the non-uniformity of microstructure and texture. Nevertheless, some traces of plastic flow are seen inside the β-grains (Fig. 12, *b*). In turn, an increase in strain rate just to 3150 s^{-1} caused fracture with partial fragmentation at one corner (Fig. 12, *c*). The microstructure formed in this case has several features that differ in various parts of the specimen. At the edges of the main crack crossing the specimen at an angle close to 45°, no traces of ASB formation were observed (Fig. 12, *d*), obviously because the parent ASB degenerated into cracks [15, 22, 42]. However, the microstructure at different edges of this crack is quite different. On the one side, the traces of several neighbouring elongated β-grains on the edge of the crack, as well as

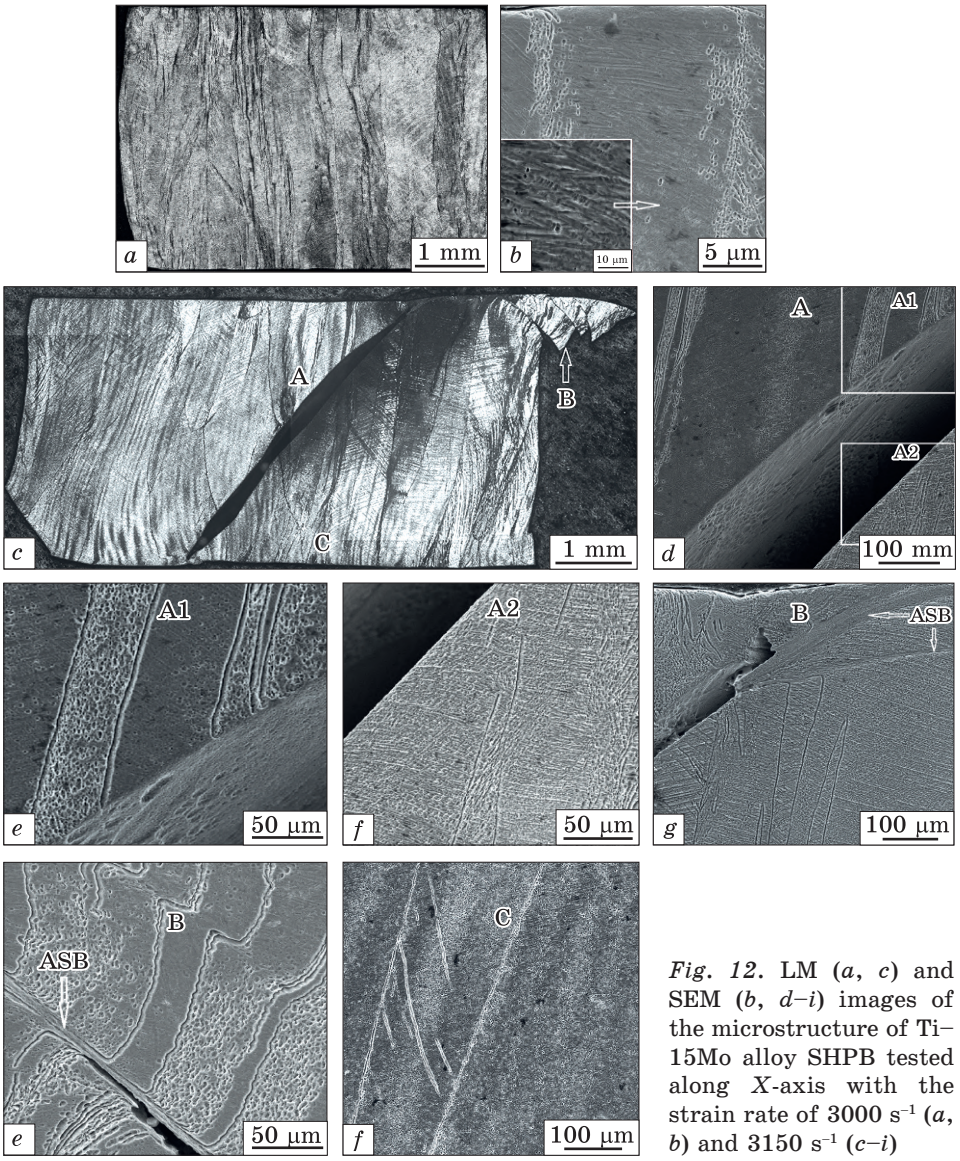

Fig. 12. LM (*a*, *c*) and SEM (*b*, *d*–*i*) images of the microstructure of Ti–15Mo alloy SHPB tested along *X*-axis with the strain rate of 3000 s^{-1} (*a*, *b*) and 3150 s^{-1} (*c*–*i*)

some traces of plastic deformation, are clearly seen, with comparatively clean surface between them (Fig. 12, *e*). Obviously, this is a result of different crystallographic orientations of these neighbouring grains. Another microstructure is observed on the opposite side of the crack (Fig. 12, *f*), that is most likely explained by different stress state in this section of the specimen.

There are no ASBs at the edges of main crack (Fig. 12, *e*–*f*); apparently, the ASBs transformed into the crack. At the same time, an ASB

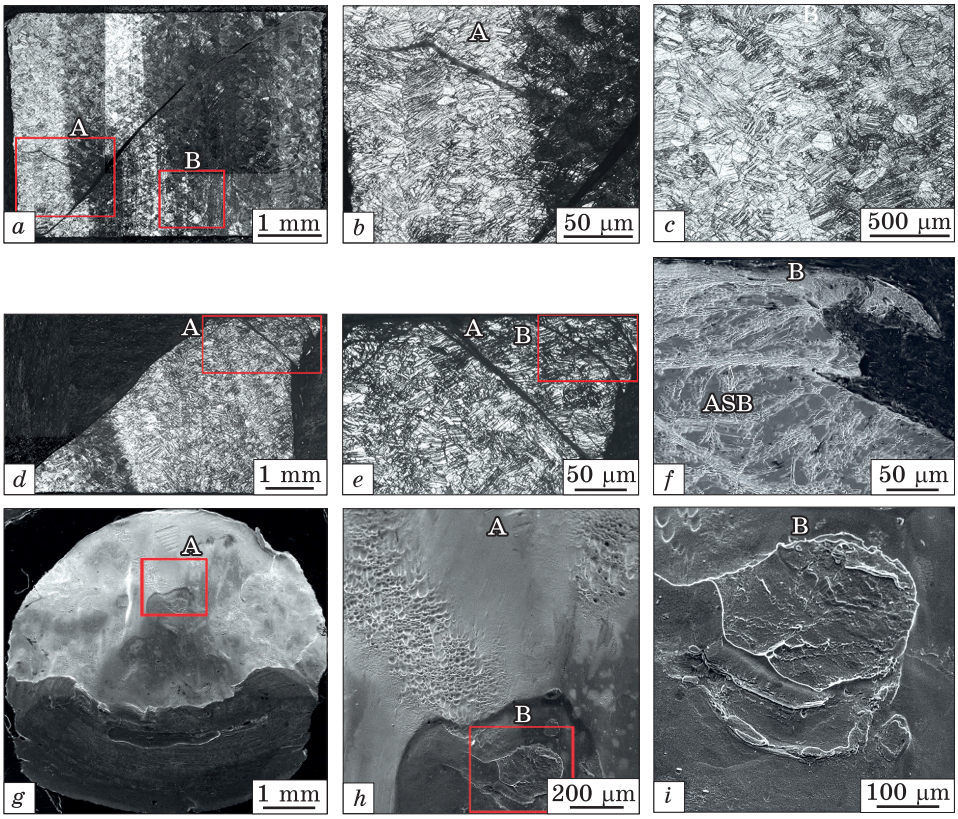

Fig. 13. Microstructure of Ti–15Mo alloy after the SHPB experiments for *Y* axis orientation with strain rates of 2930 s^{-1} (*a*) and 3280 s^{-1}, where *a*–*e* — LM images, and *f*–*i* — SEM images

was found at the tip (probable initiation site) of the main crack at the corner of the specimen (Fig. 12, *g*). In this zone, the ASB bifurcates and propagates in several divergent directions due to shear and local fragmentation (Fig. 12, *c*, *g*, *h*). In the areas remote from the main crack, the microstructure is similar to the previously considered case for lower strain rate (compare Fig. 12, *b* and *i*).

Compression along the *Y*-axis caused somewhat earlier fracture at a lower strain rate of 1930 s^{-1} (Fig. 13, *a*). Secondary cracks branching off from the main one are observed (Fig. 13, *b*). However, the β-intragrain microstructure is rather uniform across the whole sample, with rather high density of plastic deformation traces (including twins) at different directions in neighbouring grains (Fig. 13, *b*, *c*). Apparently, these directions are determined by the crystallographic orientations of the grains.

Further increase in strain rate caused main crack formation and complete fracture of the specimens (Fig. 13, *d*), as well as appearance of

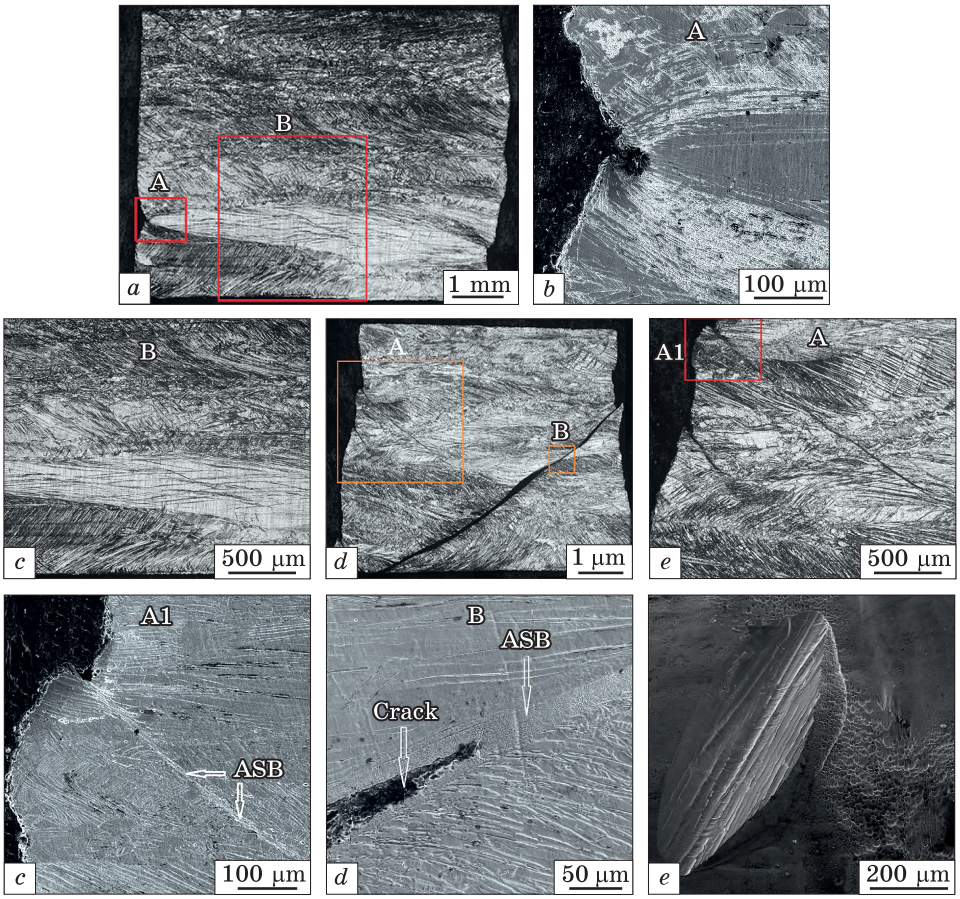

Fig. 14. Microstructure (*a*–*g*) and fracture surface (*h*) of Ti–15Mo alloy after the SHPB experiments for *Z*-axis orientation with strain rates of 2310 s^{-1} (*a*–*c*) and 2730 s^{-1} (*d*–*h*). Here, *a*, *b*, *e* — LM images; *c*, *f*–*h* — SEM images

a series of secondary cracks (Fig. 13, *e*). ASBs were observed near some secondary cracks (Fig. 13, *f*). It should be noted that no ASBs were observed along the edges of both completely formed main crack and secondary ones (including the corner of the specimen where fragmentation occurred) (Fig. 13, *d*, *e*).

Typical fracture surfaces of the specimens tested along *Y*-axis (Fig. 13, *g*) comprise of areas of ductile fracture and separation both along the elements of the intragrain substructure (Fig. 13, *h*) and directly along the boundaries of individual grains (Fig. 13, *i*). This type of fracture is also determined by the crystallographic orientations of individual grains and their subgrains relatively to external stresses; the fracture surfaces look rather similar for all specimens tested in different directions.

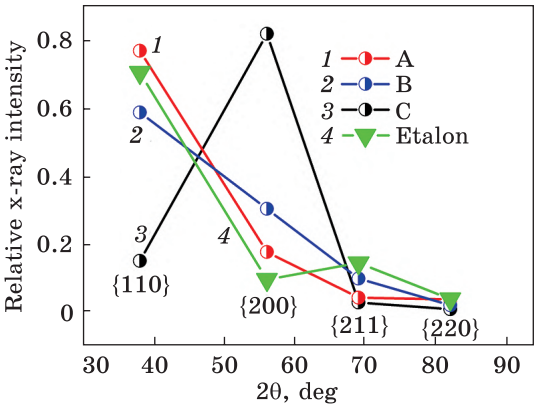

Fig. 15. Relative intensities of reflexes *vs.* 2Θ angle for the planes *A*, *B*, *C*, and for reference β-Ti with random texture

The microstructure of the specimens compressed along the *Z*-axis differs significantly from those tested along *X*- or *Y*-axis (Fig. 14). Similar to the case of quasi-static compression, the protrusions and extrusions formed on the backsides of the specimens at the junctions of neighbouring β-grains (compare Figs. 11, *e*, *f* with 14, *a*, *b*). The differences in the deformation substructure of parallel elongated neighbouring grains are also evident (Fig. 14, *b*), which is associated with the above-mentioned variations in their crystallographic texture. The secondary cracks, as well as the main crack, cross easily the boundaries between grains, despite the differences in their crystallographic orientations (Fig. 14, *e*). The ASBs were also observed in the areas close to specimen edges (Fig. 14, *f*) or outer surfaces (Fig. 14, *g*) where these cracks nucleated. In the specimens tested along the *Z*-axis, the cracks were initiated exactly on the irregularities of the lateral surface, which appeared due to the differences in the plastic deformation of adjacent β-grains.

The features of mechanical behaviour and deformational microstructure described above can be explained taking into account the crystallographic texture formed in Ti–15Mo rolled in different directions/planes (Fig. 4, *f*–*h*). As mentioned above (in Section 3.2), a {110}β texture with the fourth order symmetry was formed upon hot deformation in all three mutually perpendicular planes (*A*, *B*, and *C*). However, the 'sharpness' (intensity) of this texture is different for both these and other crystallographic planes of the β-phase lattice. Figure 15 represents the intensities of various β-phase lattice planes for *A*, *B*, and *C* surfaces of the specimen in comparison with a β-phase sample with random crystallographic texture. A comparison of these data shows that the crystallographic textures on the surfaces *A* and *B* differ little from the 'textureless' state for the reflection planes {110}, {211}, and {220}, whereas the texture is noticeably stronger for the plane {200}. As for the surface *C*, these differences are much higher, especially for the planes {110} and {200}. Moreover, a multidirectional change in the intensity of reflections relative to the 'textureless' state is observed exactly for these two crystallographic planes. Thus, one can conclude that it is this very special spatial orientation of the crystallographic lattice

of the Ti–15Mo alloy in the state #2 that leads to the above-mentioned special mechanical behaviour during dynamic compression tests in the *Z*-direction (Fig. 7, *c*). It should be emphasized that this effect of the crystallographic texture manifests only at high strain rates, which leave no time for relaxation processes.

4.3. Strain Energy

Strain energy (SE, also called tensile toughness or deformation energy, depending on the methods of testing, or nature of material, and even specimens' geometry) was used many times as a physical parameter allowing to compare the mechanical response of different structural materials tested in equivalent conditions [12, 16–21, 43]. The results of strain energy calculations for the Ti–15Mo alloy tested by quasi-static tension, quasi-static and high strain rate compressions are presented in Fig. 16, *a*, *b*, and *c*, respectively. The dependences of SE on strain rate shown in Fig. 16, *a* and *c* are rather similar to those for other titanium alloys; however, the SE values for the Ti–15Mo alloy are quite lower as compared to the two-phase alloys, such as Ti-6-4 [16, 21] and T110 [22]. A more detailed comparison will be given in the next section, here we only note that the SE values, both for the QS and high-strain rate compression, are approximately 40% lower for the Ti–15Mo alloy than for the above-mentioned two-phase $\alpha+\beta$ alloys with fully transformed uniform globular microstructure. Obviously, from the viewpoint of the achieved level of strain energy, the high ductility reached in this alloy (up to 40% in quasi-static tension; see Fig. 5) does not compensate comparatively low level of strength: 800–1000 MPa for Ti–15Mo *vs.* 1200 MPa and higher for Ti-6-4 and T110.

Under quasi-static tension along the '*X*' axis, the SE values were essentially higher for annealed and water quenched states #2 and #3 as compared with as-rolled state #1 (Fig. 16, *a*). It can also be noted that the increase in the strain rate by three orders of magnitude (from $8 \cdot 10^{-4}$ s^{-1} to $8 \cdot 10^{-1}$ s^{-1}) has very little effect on the SE value of the alloy loaded along the *X*-axis. Under quasi-static compression, regardless loading direction and the increase in strain rate by three orders of magnitude (from 0.001 s^{-1} to 1 s^{-1}), the SE values remained practically the same (Fig. 16, *b*); however, it should be taken into account that these tests were carried out only for the state #2. The state #2 specimens tested in all three directions at high strain rates had very similar SE values up to the rates about 2200 s^{-1} (Fig. 16, *c*). At higher strain rates, the SE *vs.* strain rate dependences were different completely. Besides the microstructural features considered earlier (Section 4.2), this is also explained by the above-mentioned texture. First of all, it should be mentioned that the specimens compressed along the *Z* axis (curve *3* in

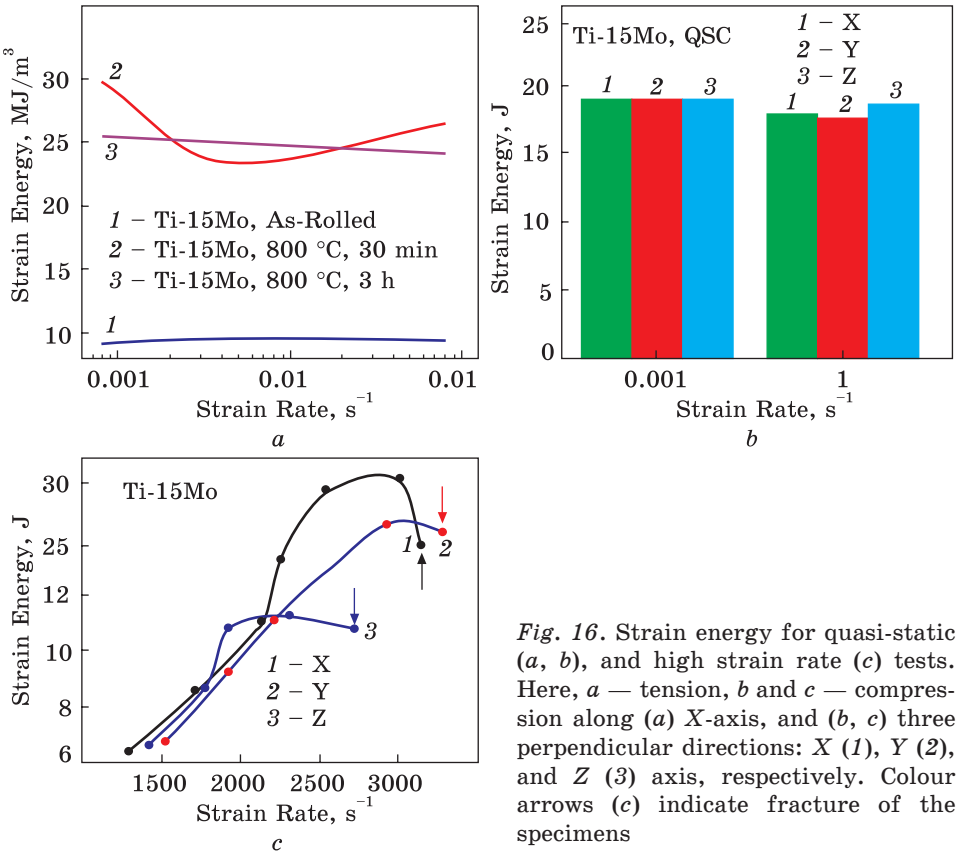

Fig. 16. Strain energy for quasi-static (*a*, *b*), and high strain rate (*c*) tests. Here, *a* — tension, *b* and *c* — compression along (*a*) *X*-axis, and (*b*, *c*) three perpendicular directions: *X* (*1*), *Y* (*2*), and *Z* (*3*) axis, respectively. Colour arrows (*c*) indicate fracture of the specimens

Fig. 16, *c*) also had lower resistance to fracture, which resulted in the lowest values of SE (10.8 J) and critical strain rate (2730 s^{-1}). These values were essentially higher for the specimens deformed in two other directions (*X*- and *Y*-axes, curves *1* and *2*, respectively).

Thus, all the above experimental results and their interpretation clearly indicate the following. Due to the tendency of titanium β-alloys to deformation localization [24], hot deformation processing of Ti–15Mo alloy caused the formation of essential inhomogeneity and anisotropy of microstructure and crystallographic texture; this effect has been also observed for some other titanium alloys [2, 44]. Such inhomogeneity, in turn, results in anisotropy of mechanical behaviour of rolled alloy. Ultimately, this anisotropy has stronger effect at high strain rates, when the material does not have enough time for relaxation processes, such as nucleation and motion of dislocations.

4.4. Comparison with Other Titanium Alloys and Some Other Structural Materials

From the standpoint of practical applications, it is important to compare the mechanical behaviour of studied Ti–15Mo alloy with other Ti-based materials, as well as with some other important structural materials. First, it should be noted that the mechanical behaviour of all materials studied in terms of strain energy is very different, depending on both strain rate and testing method (tension or compression). For example, the Ti–15Mo alloy has high SE values at quasi-static tension along two perpendicular directions *X* and *Y* (Fig. 17, *a*). Another situation is observed in the case of compression. Under quasi-static compression, the highest SE values are observed for the T110 alloy with fully transformed fine globular microstructure (Fig. 17, *b*). Obviously, the main contribution to the SE comes from the strength of alloys/materials. Under high strain-rate compression, the T110 alloy has the same SE-strain rate dependence as Ti64 (Fig. 17, *c*), which is noticeably inferior to its behaviour at quasi-static tests (Fig. 17, *b*).

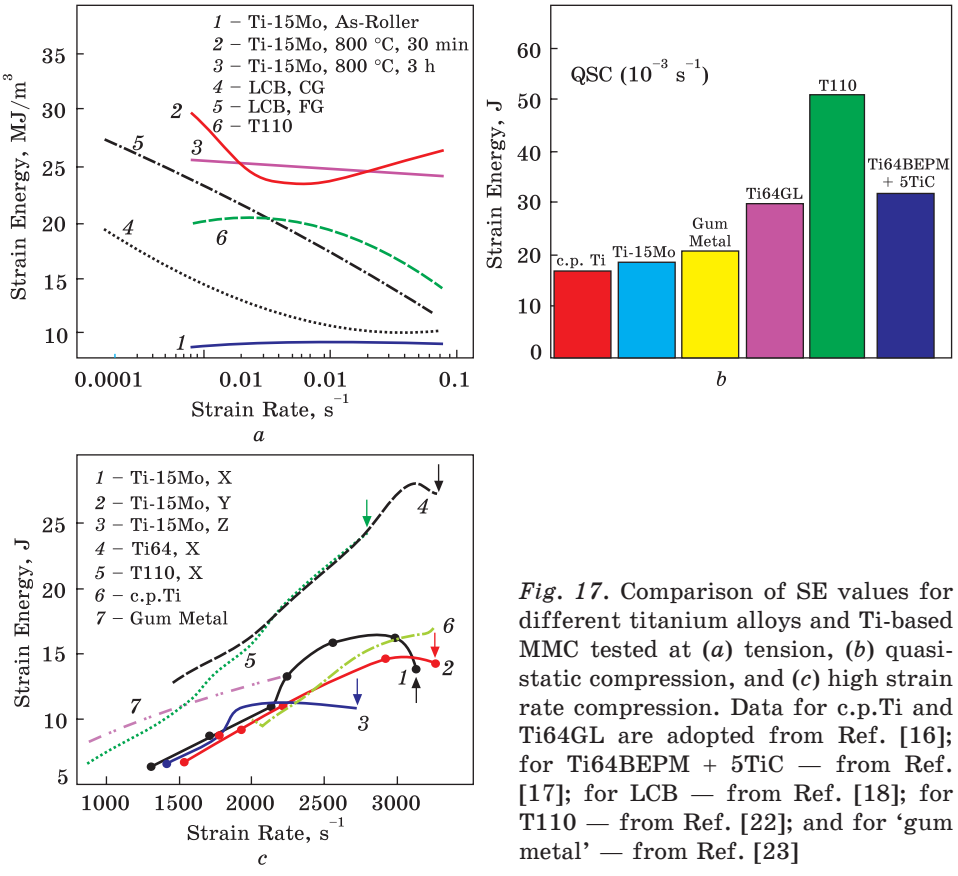

Fig. 17. Comparison of SE values for different titanium alloys and Ti-based MMC tested at (*a*) tension, (*b*) quasi-static compression, and (*c*) high strain rate compression. Data for c.p.Ti and Ti64GL are adopted from Ref. [16]; for Ti64BEPM + 5TiC — from Ref. [17]; for LCB — from Ref. [18]; for T110 — from Ref. [22]; and for 'gum metal' — from Ref. [23]

An analysis of the behaviour of various titanium alloys under high strain rate compression (Fig. 17, *c*) allows us to conclude that they can be formally divided into two groups. The first one comprises of single-phase materials: pseudo-α (h.c.p. lattice, curve *6*) c.p.Ti, and β-alloy Ti–15Mo (b.c.c. lattice, curves *1–3*); SE *vs.* strain rate dependences for these materials are very similar within a wide range of strain rates. The difference between Ti–15Mo alloy and c.p.Ti consists in the fact that the first material fractures at strain rates 2700–3300 s^{-1}, depending on the angle between the axis of crystallographic texture and applied stress, whereas pure α-titanium was unbroken up to the rate of 3400 s^{-1}. The second group includes two-phase α+β alloys Ti64GL and T110, which have SE values approximately equal to the sum of the SEs for pure α- and β-alloys on the same chart for each specific strain rate. This allows us to make a cautious assumption that, under the given test conditions, the behaviour of two-phase alloys is explained by the superposition of the contributions of phase constituents. Something similar was noted when 3-point flexure tests were compared with tension and compression of c.p.Ti and Ti64 alloy with globular microstructure in Ref. [45]: the SE values measured by the first method were approximately equal to the sum of SEs obtained by the second and third methods. In the same work, it was also noted that this 'summation' rule was not observed in most other cases that is most likely caused by a decisive influence of a number of structural and textural factors. As for the data obtained for the 'gum metal', it is somewhat out of this scheme. At relatively low strain rates, its SE values correspond to those for two-phase alloys, and they become closer to single-phase alloys as strain rate increases. However, it should be emphasised that the mechanical behaviour of this material is also very specific: it showed intense dynamic softening at all strain rates applied in Ref. [23]. At the same time, strain hardening was observed both during quasi-static and dynamic tests for all titanium alloys studied by us: *e.g.*, see Figs. 5, *b* and 7, as well as the data in Refs. [16–18, 22].

Another interesting example of comparison of the critical values of the SE and maximal strain rates of some Ti-based materials is shown in Fig. 18. This figure illustrates a comparison of the maximum SE values and the highest strain rates, at which the specimens did not fracture during dynamic tests of Ti–15Mo and some other previously studied materials based on the titanium alloy Ti-6-4. It clearly shows that although Ti–15Mo is inferior to most of other studied materials in SE_{max}, it surpasses them all in the $\dot{\varepsilon}_{max}$ except Ti64GL only, which has an exceptional combination of a uniform fine globular microstructure with a rather sharp axial texture [16]. This comparison once again shows that the main contribution to the SE level is made by the compressive strength of the material. Only a sharp drop in the overall plasticity (exactly as in the case of the Ti64 alloy with a lamellar microstructure Ti64LM) leads

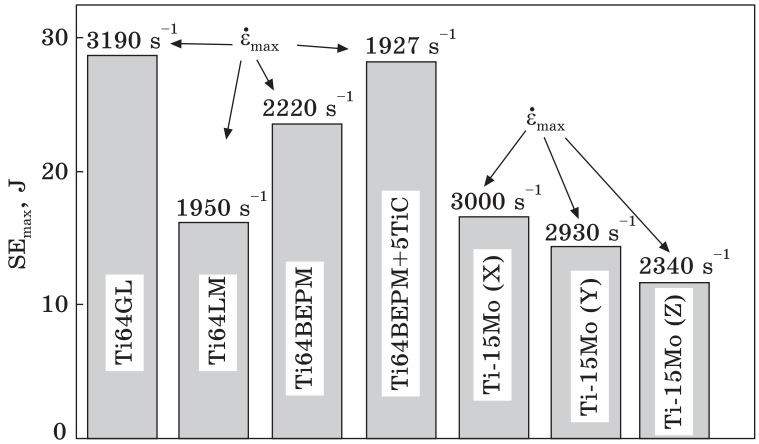

Fig. 18. Comparison of SE_{max} and $\dot{a}_{max}$ values for Ti–15Mo in the state #2 tested in three mutually perpendicular directions as compared with the data for Ti64GL, Ti64LM (adopted from Ref. [16]), Ti64BEPM, and Ti64BEPM + 5TiC (adopted from Ref. [17])

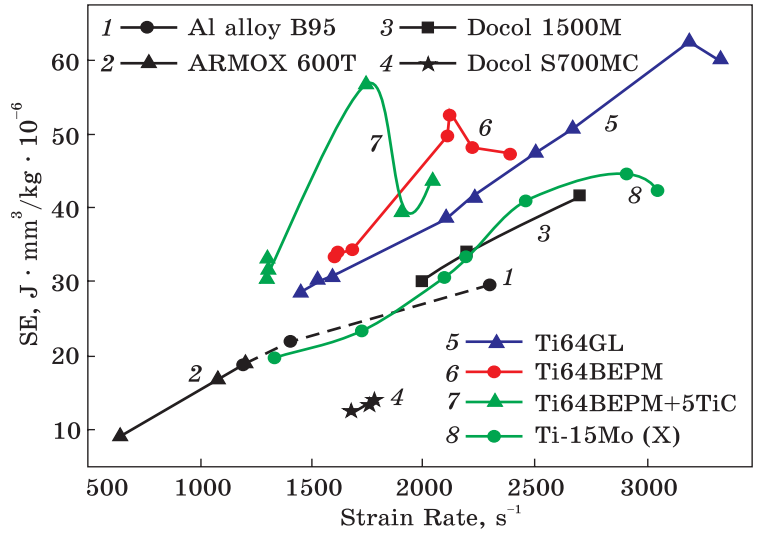

Fig. 19. Comparison of the specific SE *vs.* the strain rate for different materials. The data for curves *1–6* and *7* are adopted from Refs. [16, 17], respectively

to a decrease in its SE to a level lower than that of the Ti–15Mo alloy. In turn, the superiority in the critical strain rate ($\dot{\varepsilon}_{max}$) of the Ti–15Mo alloy over most other materials in Fig. 18 (3000 s^{-1} *vs.* 1950–2220 s^{-1}) is obviously caused by its higher ductility (of about 0.3 *vs.* 0.2).

From the practical viewpoint, it is also very interesting to compare the results obtained for the Ti–15Mo alloy with the best data for tita-

nium alloys and MMCs based on them, as well as for such important structural materials as the Al-based hardenable alloy B95 and two steels, taking into account their specific weight. Figure 19 represents a comparison of SE specific values *vs.* strain rate. It is again possible to divide formally the data shown in this figure into two groups. The first group includes the Ti-6-4 alloy with an 'ideal' globular microstructure and a sharp texture (curve *5*), the same alloy with relatively fine β-grains and fine lamellar α-phase produced by the BEPM method (curve *6*), and MMC based on it, hardened with 5% TiC particles (curve *7*); these materials have the maximum values of the specific SE. Most of the materials belong to the second group, including aluminium alloy B95, high-strength steels ARMOX 600T and Docol 1500M (curves *1*–*3*), and the studied Ti–15Mo alloy (curve *8*). Thus, we can conclude that, taking into account the specific weight, the performance of the Ti–15Mo alloy at the SHPB tests is comparable to many other structural materials and is inferior only to some very special materials based on the Ti-6-4 alloy.

Thus, Ti–15Mo alloy showed good, but not outstanding mechanical characteristics; the reason for this is the peculiarities of its microstructural and textural state formed as a result of the applied conventional production technology. It can be assumed that in the case of the formation of a more dispersed and homogeneous β-grain microstructure, for example, formed by special processing methods ensuring microstructure refinement [5, 30, 32, 46], the mechanical properties of this alloy can be significantly improved.

4.5. Deformation Mechanisms

Summarizing all the data and results of our previous studies of the effect of strain rate on the mechanical behaviour of Ti alloys and Ti-based MMCs, it is possible to suggest the following general scheme. The β-grains after rolling, annealing and water quenching are elongated in the *X*-direction and flattened along the *Z*-axis, they resemble cylinders or 'barrels' (Fig. 20, *a*). The β-grains in the compressed specimens are elongated along the *X*-axis, somewhat expanded along the *Y*-axis, and flattened along the *Z*-axis, as schematically shown in locations *I* in Fig. 20, *b*, *d*, and *f*, respectively. Compression along the *X*-axis, *i.e.*, in the direction of longest dimension of the elongated β-grains (for some simplification, the scheme shows the initial shape of the samples as cubes), led to somewhat inhomogeneous deformations, depending on the location of these grains in the specimen. Grains located closer to the lateral side of the specimen (like β-grains *I*, *II*, and *III* in Fig. 20, *b*, location *I*) predominantly bend along with the nearest free surface of the specimen (location *II* in Fig. 20, *b*). At the same time, the grains located closer to the centre of the specimen either bend and wriggle in

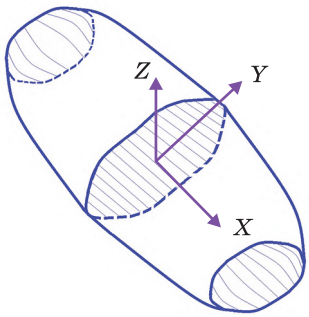

a

Fig. 20. Schematic presentation of the β-grains' shape in the initial state (*a*). Influence of initial β-grains' spatial orientation (*I*) with respect to the applied compressing force (*F*) on the mode of their deformation upon testing (*II*) along the *X* (*b*), *Y* (*d*), and *Z* (*f*) axes. The crack nucleation sites under the compression along *X* (*c*), *Y* (*e*), and *Z* (*g*) axis

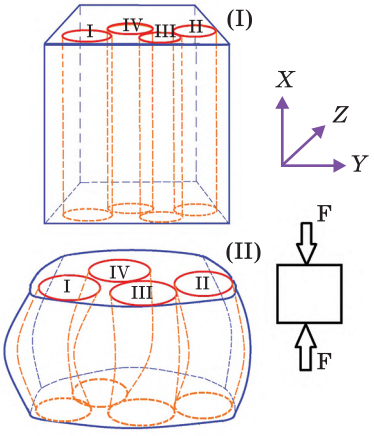

b

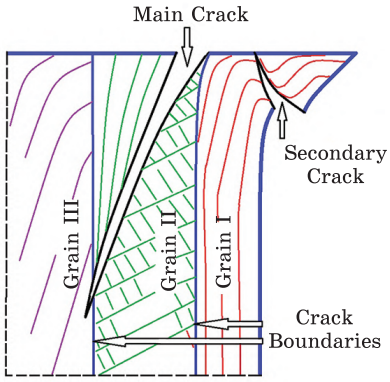

c

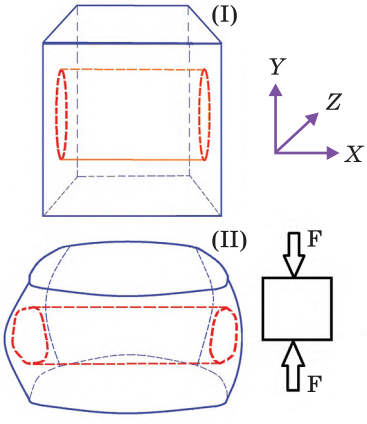

d

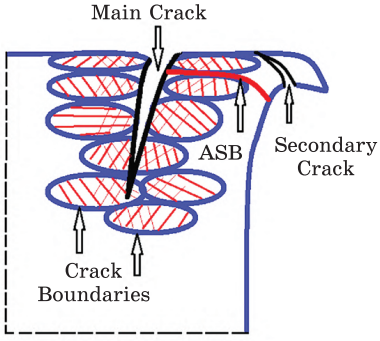

e

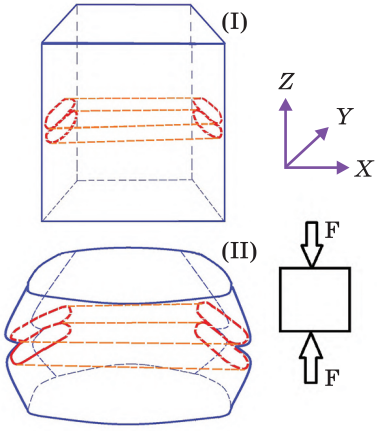

f

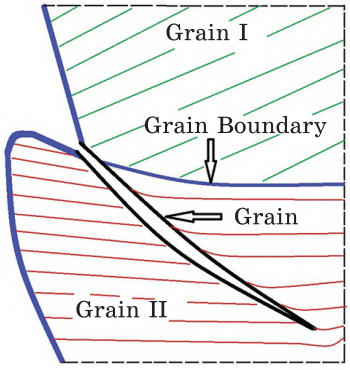

g

different directions, or take a barrel-like shape like the specimen as a whole (grain *IV* in Fig. 20, *b*, location *II*). Under high strain rate compression, the main cracks nucleate on the grain boundaries between neighbouring grains with high misorientation, in the locations where the stress produced by the external force reaches values sufficient for crack initiation (Fig. 20, *c*). After nucleation, the main crack propagates through the grains, without significant deviations at the grain boundaries. Secondary cracks appear in the different parts of the specimen, where the temperature significantly rises due to local deformation, and local stresses exceed certain limits. It should also be emphasized that the deformation substructure is significantly different at the opposite edges of the main crack (see also Fig. 12, *e*–*g*). This is most likely a consequence of different modes of stress relaxation not only in different parts of a split grain, but also in opposite parts of the specimen.

Compression along the *Y*-axis in general caused shortening of the β-grains across the second longest dimension (Fig. 20, *d*). Since the adjacent grains along this axis do not have high misorientation, the material plastically flows in a rather uniform and cooperative manner. At the same time, the shape of β-grains in the 'cross section' changes from elongated in the vertical direction towards more flattened in the plane parallel to the plane of applied load (Fig. 20, *d*, *e*). Cracks nucleate also on the boundaries between adjacent grains near the contact surface of the SHPB bars, where local stresses are higher (Fig. 20, *e*). Obviously, the ASBs form here before the appearance of cracks (see also Fig. 13, *g*).

The deformation process along the '*Z*' axis is very different from the two previous cases. At first glance, it seems that in this case the β-grains would just continue to elongate and flatten, as it was during previous rolling. However, the neighbouring grains plastically flow with different degrees of deformation. This is explained by several reasons. The first one is the differences in the misorientation and in the degree of relaxation and recrystallization completeness during annealing. It is possible that these differences were also exacerbated by the transition from rolling to uniaxial compression. The second reason consists in the peculiarities of the micro- and substructure of grains, *i.e.*, the uniformity of deformation of the grains differed significantly too through their cross section. The result of the joint influence of these factors is a lower compatibility of plastic flow along the *Z*-axis between neighbouring β-grains. Therefore, extrusions and intrusions formed on the side surfaces of the specimen (Fig. 20, *f*). The former corresponded to the central parts of the grains that have undergone maximum plastic flow, and the latter corresponded to the near-boundary zones of neighbouring grains (see Fig. 14, *b*). In the cases, where the values of plastic deforma-

tion of neighbouring grains differed mostly, a step on the surface of the specimen formed at the grain boundary due to the displacement of the grains to each other (Fig. 14, *f*). Exactly these steps are the sites of the easiest crack initiation. A crack then continues to propagate through the grain interior under the action of maximum stresses directed according to Schmid's law (Fig. 20, *g*). However, it should be noted that in this case, in contrast to compression along the *X* and *Y* axes, the formation of main cracks on the free surface near the corner of the specimens (where maximum stresses act) was not observed (Fig. 14, *e*–*f*). This indicates that the formation of the steps (acting as stress concentrators) on the side surfaces is the most important factor leading to fracture of the specimens at lower strain rates (curve *3* versus curves *1* and *2* in Fig. 17, *c*).

Thus, summarizing the obtained results, we can conclude that during compression at high strain rates of the Ti–15Mo alloy with an incompletely recrystallized banded microstructure, stress localization and subsequent crack initiation practically always occur at the β-grain boundaries. Compression along the longitudinal *X*- and transverse *Y*-axes in the rolling plane led to higher mechanical properties as compared to the *Z*-axis that is normal to the rolling plane. This is obviously explained by a specific crystallographic texture formed in the Ti–15Mo alloy upon rolling.

Finally, it should be noted that the difference between compression with quasi-static and high strain rates consists in the feasibility of stress relaxation that prevented cracking at lower rates. In the order of decreasing strain rate sensitivity, the directions of the Ti–15Mo alloy in as-rolled and non-uniform state (with respect to rolling conditions) can be arranged as follows: most sensitive is direction *Z*, then *Y*, and least sensitive is *X*. In addition, embrittlement of the β-alloys can be caused by the β-phase decomposition during application of external deforming load. Such situation ($\beta \rightarrow \alpha''$ transformation) was observed in metastable β-alloy VT22 on quasi-static deformation [23], as well as appearance of deformational α″-martensite in two-phase low alloyed Ti-6-4 alloy on dynamic compression [16]. The formation of an embrittling athermal ω-phase is also not excluded [24]. However, in this work, we did not observe the decay of the β-phase possibly due to the insufficient sensitivity of the used research methods.

5. Conclusions

Obtained experimental results, their discussion and comparison with earlier data allow us to conclude as follow below.

• Application of conventional metallurgical cast and wrought approach to the production of Ti–15Mo alloy causes formation of non-

uniform laminated microstructure and specific crystallographic texture in the direction normal to rolling plane. This is explained by the strong tendency of the β-alloys to localized deformation, which is also promoted by the relatively low temperature of phase transformation (temperature T_β). Presumably, the mechanical properties of the alloy can be improved significantly by forming finer and more homogeneous β-grain microstructure.

• Under quasi-static loading conditions, the above features of the microstructure and crystallographic texture have a relatively small negative effect on the mechanical properties of the Ti–15Mo alloy. In terms of strength, ductility, and strain energy, the tested material has a balance of mechanical properties very close to those for other single-phase (alpha or beta) titanium alloys tested under the same loading conditions. This is obviously explained by sufficient time for the relaxation processes to occur during plastic deformation, as well as by the stability of the β-phase to decomposition.

• Specific features of the inhomogeneous streaky microstructure, as well as the texture of the Ti–15Mo alloy, noticeably affect its mechanical behaviour under dynamic loading. The effect strongly depends on the orientation of loading direction with respect to rolling plane and direction. Thus, the intensity of plastic flow is strongly affected by the spatial orientation of β-grains. The cracks are usually initiated at the boundaries between neighbouring grains with comparatively high misorientation. A specific texture has additional effect and accelerates cracking under loading in the direction normal to the rolling plane at lower strain rates.

• Despite the mechanical properties of Ti–15Mo correspond to those of other single-phase titanium materials (like commercial purity titanium and some other β-alloys), taking into account its specific weight, it is not inferior in certain properties (*e.g.*, specific deformation energy) to other materials, and it can be used in the armouring systems, for example, as a part of multilayered structures.

Acknowledgements. The present studies were carried out according to the Agreement of Cooperation between the G.V. Kurdyumov Institute for Metal Physics of the N.A.S. of Ukraine and the Jarosław Dąbrowski Military University of Technology, Poland. Some separate works were financed by the N.A.S. of Ukraine within the framework of the research project #III-09-18.

APPENDIX: List of Acronyms

Acronym	Term
Ti–15Mo	Ti–15(wt.%)Mo alloy
Ti-6-4 (Ti64)	Ti–6(wt.%)Al–4V alloy
Ti64CL	Ti-6-4 alloy with microstructure of globular morphology [16]
Ti64PL	Ti-6-4 alloy with microstructure of lamellar morphology [16]
Ti64BEPM	Ti-6-4 alloy produced with blended elemental powder metallurgy method [17]
Ti64BEPM + + 5TiC	Metal matrix composite on the base of Ti-6-4 alloy reinforced with 5 vol.% of TiC particles produced with blended elemental powder metallurgy method [17]
c.p.Ti	Commercial purity titanium
α	Low temperature h.c.p. phase of titanium and its alloys
β	High temperature b.c.c. phase of titanium and its alloys
T_β	Beta-transition temperature — equilibrium temperature of $\alpha + \beta_0 \rightarrow \beta$ polymorphous transformation, *i.e.*, temperature of the boundary between $\alpha + \beta$ and β fields on phase diagram
FH	Furnace heating
AC	Air cooling
WQ	Water quenching
QS	Quasi static conditions of mechanical tests
QST	Quasi static tension
QSC	Quasi static compression
SHPB	Split Hopkinson pressure bar method of high strain rate testing
UTS	Ultimate tensile strength
YS	Yield strength
REl	Relative elongation
RA	Reduction in area
LM	Light (optical) microscopy
SEM	Scanning electron microscopy
SEI	Secondary electron image (SEM)
BEI	Backscattered electron image (SEM)
EBSD	Electron back scattering diffraction (SEM)
GCM	Grain contours map (EBSD)
CSR	Coherent scattering region
FWHM	Full width on half height of maximum of x-ray reflections
TEM	Transmission electron microscopy
XRD	X-ray diffraction
SADP	Selected area diffraction pattern
SE	Strain energy
SE_{max}	Maximal strain energy value obtained on SHPB impact tests at maximal strain rate
$\dot{\varepsilon}_{max}$	Maximal strain rate at which specimens did not fracture during the SHPB tests

REFERENCES

1. U. Zwicker, *Titan und Titanlegierungen* (Berlin: Springer: 1974); https://doi.org/10.1007%2F978-3-642-80587-5
2. G. Lutjering and J.C. Williams, *Titanium* (Berlin: Springer: 2007); https://doi.org/10.1007/978-3-540-73036-1
3. P.J. Bania, Beta titanium alloys and their role in the titanium industry, *Beta Titanium Alloys in the 90's* (Warrendale, PA: TMS Publications: 1993), p. 3.
4. R.R. Boyer and R.D. Briggs, *J. Mater. Eng. Perform.*, **14**: 681 (2005); https://doi.org/10.1361/105994905X75448
5. O.M. Ivasishin, P.E. Markovsky, Yu.V. Matviychuk, S.L. Semiatin, C.H. Ward, and S.A. Fox, *J. Alloys and Compounds*, **457**, Nos. 1–2: 296 (2008); https://doi.org/10.1016/j.jallcom.2007.03.070
6. K.B. Panda and K.S. Ravi Chandran, *Metall. Mater. Trans. A*, **34**, No. 6: 1371 (2003); https://doi.org/10.1007/s11661-003-0249-z
7. S. Li, K. Kondoh, H. Imai, B. Chen, L. Jia, J. Umeda, and Y. Fu, *Materials & Design*, **95**: 127 (2016); https://doi.org/10.1016/j.matdes.2016.01.092
8. M. Nutt, V. Jablokov, H. Freese, and M. Richelsoph, *ASTM International STP 1471, 'Titanium, Niobium, Zirconium, and Tantalum for Medical and Surgical Applications' (December, 2005)* (Ed. M.J. Kraay), p. 84; https://www.astm.org/stp1471-eb.html
9. J.R.S. Martins Junior, R.A. Nogueira, R.O. de Araujo, T.A.G. Donato, V.E. Arana-Chavez, A.P.R.A. Claro, J.C.S. Moraes, M.A.R. Buzalaf, and C.R. Grandini, *Mat. Res.*, **14**, No. 1 (2011); https://doi.org/10.1590/S1516-14392011005000013
10. Sh. Xu, Ch. Zhou, Y. Liu, B. Liu, and K. Li, *J. Alloys and Compounds*, **738**: 188 (2018); https://doi.org/10.1016/j.jallcom.2017.12.124
11. S. Zherebtsov, M. Ozerov, E. Povolyaeva, V. Sokolovsky, N. Stepanov, D. Moskovskikh, and G. Salishchev, *Metals*, **10**: 40 (2020); https://doi.org/10.3390/met10010040
12. P.E. Markovsky, S.V. Akhonin, V.A. Berezos, O.O. Stasyuk, O.P. Karasevska, and I.M. Gavrysh, *Metallogr. Microst. Anal.*, **9**: 856 (2020); https://doi.org/10.1007/s13632-020-00705-7
13. S.V. Akhonin, F.N. Pikulin, V.A. Berezos, D.V. Kovalchuk, and S.B. Tugai, *Electrometallurgy Today*, No. 3: 15 (2019); https://doi.org/10.15407/sem2019.03.03
14. H. Kolsky, *J. Sound and Vibration*, **1**, No. 1: 88 (1964); https://doi.org/10.1016/0022-460X(64)90008-2
15. W. Chen and B. Song, *Split Hopkinson (Kolsky) Bar: Design, Testing and Applications* (Berlin: Springer: 2011); https://doi.org/10.1007/978-1-4419-7982-7
16. P.E. Markovsky, J. Janiszewski, V.I. Bondarchuk, O.O. Stasyuk, M.A. Skoryk, D.G. Savvakin, K. Cieplak, P. Dziewit, and S.V. Prikhodko, *Metals*, **10**, No. 11: 1404 (2020); https://doi.org/10.3390/met10111404
17. P.E. Markovsky, J. Janiszewski, O.O. Stasyuk, V.I. Bondarchuk, D.G. Savvakin, K. Cieplak, D. Goran, P. Soni, and S.V. Prikhodko, *Materials*, **14**, No. 22: 6837 (2021); https://doi.org/10.3390/ma14226837

18. P.E. Markovsky, Yu.V. Matviychuk, and V.I. Bondarchuk, *Mater. Sci. Eng. A*, **559**: 782 (2013);
https://doi.org/10.1016/j.msea.2012.09.024
19. P.E. Markovsky, V.I. Bondarchuk, and O.M. Herasymchuk, *Mater. Sci. Eng. A*, **645**: 150 (2015);
https://doi.org/10.1016/j.msea.2015.08.009
20. P.E. Markovsky, V.I. Bondarchuk, O.V. Shepotinnyk, and I.M. Gavrysh, *Metallofiz. Noveishie Tekhnol.*, **38**, No. 7: 935 (2016);
https://doi.org/10.15407/mfint.38.07.0935
21. P.E. Markovsky and V.I. Bondarchuk, *J. Mater. Eng. Perform.*, **26**, No. 7: 3431 (2017);
https://doi.org/10.1007/s11665-017-2781-9
22. P.E. Markovsky, J. Janiszewski, O.O. Stasyuk, V.I. Bondarchuk, K. Cieplak, and O.P. Karasevska, *Metallogr. Microstruct. Anal.*, **10**: 839 (2021);
https://doi.org/10.1007/s13632-021-00797-9
23. K.M. Golasinski, J. Janiszewski, J. Sienkiewicz, T. Plocinski, M. Zubko, P. Swiec, and E.A. Pieczyska, *Metal. Mater. Trans. A*, **52**: 4558 (2021);
https://doi.org/10.1007/s11661-021-06409-z
24. I. Weiss and S.L. Semiatin, *Mater. Sci. Eng. A*, **243**: 46 (1998);
https://doi.org/10.1016/S0921-5093(97)00783-1
25. O.P. Karasevska, O.M. Ivasishin, S.L. Semiatin, and Yu.V. Matviychuk, *Mater. Sci. Eng. A*, **354**: 121 (2003);
https://doi.org/10.1016/S0921-5093(02)00935-8
26. F.J. Humphreys and M. Hatherly, *Recrystallization and Related Annealing Phenomena* (Oxford: Pergamon: 2002);
https://doi.org/10.1016/B978-0-08-044164-1.X5000-2
27. J.E. Burke and D. Turnbull, Recrystallization and grain growth, *Progress in Metal Physics*, vol. **3**, p. 220 (1952);
https://doi.org/10.1016/0502-8205(52)90009-9
28. F.J. Humphreys and M. Hatherly, *Recrystallization and Related Annealing Phenomena* (Oxford: Pergamon: 2004);
https://doi.org/10.1016/B978-0-08-044164-1.X5000-2
29. O.M. Ivasishin, P.E. Markovsky, D.G. Savvakin, O.O. Stasiuk, V.A. Golub, V.I. Mirnenko, S.H. Sedov, V.A. Kurban, and S.L. Antonyuk, Microstructure and properties of titanium-based materials promising for antiballistic protection, *Prog. Phys. Met.*, **20**, No. 2: 285 (2019);
https://doi.org/10.15407/ufm.20.02.285
30. O.M. Ivasishin, P.E. Markovsky, D.G. Savvakin, O.O. Stasiuk, and S. Prikhodko, *Proc. 14th World Conference on Ti (10–15 June, 2019, Nantes, France)* (MATEC Web of Conferences), vol. **321**, p. 11028 (2020);
https://doi.org/10.1051/matecconf/202032111028
31. O.M. Ivasishin, P.E. Markovsky, D.G. Savvakin, O.O. Stasyuk, S.D. Sitzman, M. Norouzi Rad, and S. Prikhodko, *J. Mater. Process. Technol.*, **269**: 172 (2019);
https://doi.org/10.1016/j.jmatprotec.2019.02.006
32. P.E. Markovsky, O.M. Ivasishin, D.G. Savvakin, V.I. Bondarchuk, and S. Prikhodko, *J. Mater. Eng. Perform.*, **28**, No. 9: 5772 (2019);
https://doi.org/10.1007/s11665-019-04263-0
33. J.M. Bennett, E.J. Pickering, J.S. Barnard, D. Rugg, H.J. Stone, and N.G. Jones, *Mater. Characteriz.*, **142**: 523 (2018);
https://doi.org/10.1016/j.matchar.2018.06.017

34. K. Bartha, J. Stráský, A. Veverková, J. Veselý, and M. Janeček, *Mater. Lett.*, **309**: 131276 (2022);
https://doi.org/10.1016/j.matlet.2021.131376
35. G.K. Williamson and W.H. Hall, *Acta Metall.*, **1**: 22 (1953);
https://doi.org/10.1016/0001-6160(53)90006-6
36. M. Marciszko, *Diffraction Study of Mechanical Properties and Residual Stresses Resulting from Surface Processing of Polycrystalline Materials* (Ph.D. Thesis) (Ecole Nationale Supйrieure d'Arts et Métiers, Paris; University of Science and Technology, Krakow: 2013);
https://pastel.archives-ouvertes.fr/pastel-00992073
37. Z. Chen, Y. Yang, and H. Jiao, Some Applications of Electron Back Scattering Diffraction (EBSD) in Materials Research, *Scanning Macroscopy* (Ed. V. Kazmiruk) (Rijeka: INTECH: 2012), p. 55;
https://doi.org/10.5772/35267
38. B. Qian, M. Yang, L. Lilensten, P. Vermaut, F. Sun, and F. Prima, *Mater. Res. Lett.*, **10**, No. 2: 45 (2022);
https://doi.org/10.1080/21663831.2021.2013967
39. P.E. Markovsky, V.I. Bondarchuk, Yu.V. Matviychuk, and O.P. Karasevska, *Trans. Nonferrous Met. Soc. China*, **24**, No. 5: 1365 (2014);
https://doi.org/10.1016/S1003-6326(14)63200-3
40. S. Ozan, Yu. Li, J. Lin, Ya. Zhang, H. Jiang, and C. Wen, *Mater. Sci. Eng. A*, **719**, No. 14: 112;
https://doi.org/10.1016/j.msea.2018.02.034
41. I.S. Aliiev, I.G. Zhbankov, L.V. Tagan, and A.A. Shvets, *Obrabotka Materialov Davleniem*, No. 1 (34): 50 (2013) (in Russian);
http://www.dgma.donetsk.ua/science_public/omd/omd_1(34)_2013/article/13AISFLF.pdf
42. Y.-X. Du, X.-L. Yang, Z.-S. Li, F. Hao, Y.-C. Mao, S.-Q. Li, X.-H. Liu, Y. Feng, and Z.-M. Yan, *Trans. Nonferrous Met. Soc. China*, **31**: 1641 (2021);
https://doi.org/10.1016/S1003-6326(21)65604-2
43. *Tensile Testing* (Ed. J.R. Davis) (Materials Park, Ohio: ASM International: 2004).
44. S.L. Semiatin, *Metall. Mater. Trans. A*, **51**, No. 6: 2593 (2020);
https://doi.org/10.1007/s11661-020-05625-3
45. P.E. Markovsky, *Mater. Sci. Forum*, **941**: 1384 (2018);
https://doi.org/10.4028/www.scientific.net/MSF.941.1384
46. Q.V. Viet, A.A. Gazder, A.A. Saleh, P.E. Markovsky, O.M. Ivasishin, and E.V. Pereloma, *J. Alloys and Compounds*, **585**, No. 1: 245 (2014);
https://doi.org/10.1016/j.jallcom.2013.09.122

Received 12.04.2022;
in final version, 20.06.2022

П.Є. Марковський[1,2], *Я. Янішевський*[2], *С.В. Ахонін*[3], *В.І. Бондарчук*[1], *В.О. Березос*[3], *К. Чеплак*[2], *О.П. Карасевська*[1,4], *М.А. Скорик*[1]

[1] Інститут металофізики ім. Г.В. Курдюмова НАН України, бульв. Академіка Вернадського, 36, 03142 Київ, Україна

[2] Військовий технічний університет ім. Ярослава Данбровського, вул. Генерала Сильвестра Каліського, 2, 00-908 Варшава, Польща

[3] Інститут електрозварювання ім. Є.О. Патона НАН України, вул. Казимира Малевича, 11, 03150 Київ, Україна

[4] Національний технічний університет України «Київський політехнічний інститут імені Ігоря Сікорського», просп. Перемоги, 37, 03056 Київ, Україна

МЕХАНІЧНА ПОВЕДІНКА СТОПУ Ti–15Mo, ВИГОТОВЛЕНОГО МЕТОДОМ ЕЛЕКТРОННО-ПРОМЕНЕВОГО ХОЛОДНОГО ГОРНОВОГО ТОПЛЕННЯ, ЗАЛЕЖНО ВІД ШВИДКОСТИ ДЕФОРМАЦІЇ У ПОРІВНЯННІ З ІНШИМИ ТИТАНОВИМИ СТОПАМИ

Стоп Ti–15 (мас.%) Mo було виготовлено традиційним методом лиття та деформації з використанням подвійного електронно-променевого холодного подового топлення, 3*D*-гарячого пресування та подальшого вальцювання. Три партії зразків було піддано дослідженню мікроструктури та квазистатичним випробуванням на розтягання в наступних станах: (1) у стані прокатки, (2) частково перекристалізованому шляхом відпалу за 800 °C протягом 40 хвилин, (3) відпаленому за 800 °C протягом 3 годин з наступним гартуванням у воду для фіксації β-стану. Зразки в стані (2) було обрано для більш детального вивчення механічної поведінки як за квазистатичного, так і за високошвидкісного стискання. Одержані дані про механічну поведінку проаналізовано стосовно впливу вихідної мікроструктури та кристалографічної текстури в трьох взаємно перпендикулярних площинах на енергію деформації та критичну швидкість деформації, яка призводить до руйнування. Детальне вивчення мікроструктури досліджуваних зразків виявило вплив вихідної структури та текстури на механізми деформації за різних швидкостей деформації. Відзначено визначальний ефект мікроструктурної неоднорідности та кристалографічної текстури, що утворюється під час вальцювання. Результати порівнюються з результатами, одержаними раніше для інших титанових стопів і деяких важливих конструкційних матеріалів, випробуваних у тих же умовах. Показано, що стоп Ti–15Mo має достатньо високі механічні характеристики. За високих швидкостей деформації цей матеріал відповідає іншим однофазним титановим стопам за енергією деформації; одначе він поступається двофазним стопам з дисперсною й однорідною мікроструктурою, наприклад Ti-6-4 або T110 (див. перелік скорочень у Додатку). Враховуючи питому вагу матеріалів, стоп Ti–15Mo не поступається таким високоміцним матеріалам як термозміцнювальний стоп B95 та сталі ARMOX 600T і Docol 1500M, а також є дешевшим за інші титанові β-стопи.

Ключові слова: бета-сплав титану, мікроструктура, кристалографічна текстура, механічні властивості, деформація з різними швидкостями, механізм деформації.